On the Composition of LiNi$_{0.5}$Mn$_{1.5}$O$_4$ Cathode Active Materials

Pirmin Stüble,* Valeriu Mereacre, Holger Geßwein, and Joachim R. Binder*

LiNi$_{0.5}$Mn$_{1.5}$O$_4$ (LNMO) cathode active materials for lithium-ion batteries have been investigated for over 20 years. Despite all this effort, it has not been possible to transfer their favorable properties into applicable, stable battery cells. To make further progress, the research perspective on these spinel type materials needs to be updated and a number of persisting misconceptions on LNMO have to be overcome. Therefore, the current knowledge on LNMO is summarized and controversial points are addressed by detailed considerations on the composition and crystallography of LNMO. The findings are supported by an in-situ high temperature X-ray diffraction study and the investigation of four different types of LNMO materials, including Mn(III) rich ordered LNMO, and disordered LNMO with low Mn(III) content. It is shown that the importance of cation order is limited to a small composition range. Furthermore, new evidence contradicting the idea of oxygen defects in LNMO is presented and an enhanced classification of LNMO based on the Ni content of the spinel phase is proposed. Moreover, a balanced chemical equation for the formation of LNMO is presented, allowing for comprehensive calculations of key properties of LNMO materials. Finally, suitable target compositions and calcination programs are suggested to obtain better LNMO materials.

1. Introduction

LiNi$_{0.5}$Mn$_{1.5}$O$_4$ (LNMO) materials have excellent properties as cathode active materials for Li-ion batteries, such as a theoretical capacities up to 146.8 mAh g^{-1} and a high nominal voltage of 4.7 V (vs. Li/Li$^+$). According to LiNi$^{II}_{0.5}$Mn$^{IV}_{1.5}$O$_4$ $\rightleftarrows$ Ni$^{IV}_{0.5}$Mn$^{IV}_{1.5}$O$_4$ + Li$^+$ + e^-, LNMO can be fully delithiated and lithiated during charging and discharging without note-

worthy structural damage.[1] A characteristic advantage over state-of-the-art Ni-rich cathode active materials such as LiNi$_{0.6}$Co$_{0.2}$Mn$_{0.2}$O$_2$ (NCM-622) or LiNi$_{0.8}$Co$_{0.1}$Mn$_{0.1}$O$_2$ (NCM-811) is that LNMO is cobalt free and the redox capacity of nickel is used in its entirety. The latter could become more important considering rising nickel prices. Based on realistic full cell capacities of 120 mAh g^{-1} for LNMO and 170 mAh g^{-1} for the NCM materials, 43.8 Ah per mol Ni is obtained for LNMO, whereas NCM-622 and NCM-811 only yield 27.5 and 20.7 Ah mol^{-1}, respectively. The specific energy density of LNMO vs. graphite full cells is likewise highly competitive. For LNMO, up to 464 Wh kg^{-1} are expected, which exceeds the energy densities of corresponding NCM-622 and NCM-811 cells, yielding 416 and 448 Wh kg^{-1}, respectively.[2] Despite these favorable features, commercialization of LNMO cathode materials never succeeded. Up to date, it was not possible to build competitive cells with graphite anodes, as the degradation of these full cells has not been brought under control.[3,4] The problem, however, is not the stability of LNMO itself, but the dissolution and disproportionation of Mn(III) from LNMO, which leads to continuous decomposition reactions on the anode side and ongoing loss of cyclable lithium.[3,5,6] LNMO is nevertheless a very stable cathode material, which does not tend to decompose or release oxygen during cycling.[7]

There is scientific consensus that LNMO crystallizes as an ordered or disordered spinel phase in the space groups $P4_332$ or $Fd\overline{3}m$, respectively, or as intermediate, partial ordered phases. The term "order" refers to the distribution of transition metal cations on the octahedral sites of the spinel structure. In the ordered structure, Mn and Ni predominantly occupy the Wyckoff positions 12d and 4a, while in the disordered structure, they are statistically distributed over the 16c octahedral site.[8,9] Whether an LNMO material is predominantly ordered or disordered is commonly associated with the calcination temperature. Temperatures below 730 °C are reported to favor the formation of the ordered phase, whereas at higher temperatures disordered crystal structures are reported to occur.[10]

LNMO phases with the composition LiNi$_{0.5}$Mn$_{1.5}$O$_4$, where Mn is Mn(IV) exclusively, are reported to be obtained by calcining LNMO materials at 700 °C.[11] Increasing calcination temperatures however, lead to a partial reduction of Mn(IV) to Mn(III), which becomes obvious from an increasing Mn^{3+}/Mn^{4+}

P. Stüble, V. Mereacre, H. Geßwein, J. R. Binder
Institute for Applied Materials
Karlsruhe Institute of Technology
76344 Eggenstein-Leopoldshafen, Germany
E-mail: pirmin.stueble@kit.edu; joachim.binder@kit.edu
P. Stüble
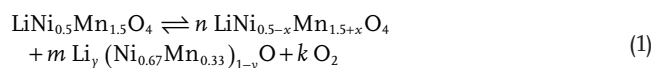Helmholtz Institute Ulm
89081 Ulm, Germany

ADVANCED
SCIENCE NEWS

www.advancedsciencenews.com
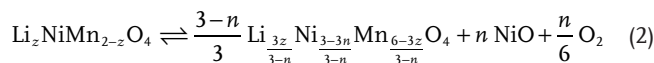
ADVANCED
ENERGY
MATERIALS

www.advenergymat.de

redox plateau around 4 V in the charge and discharge voltage profiles. In literature two different explanations for the formation of Mn(III) in LNMO are discussed. According to a common notion, oxygen is released from the LNMO phase, leading to the composition $LiNi_{0.5}Mn_{1.5}O_{4-\delta}$, or, more precisely $LiNi_{0.5}^{II}Mn_{1.5-2\delta}^{IV}Mn_{2\delta}^{III}O_{4-\delta}$, where δ is roughly 0 to 0.7. A prominent and frequently cited work advocating oxygen defects in LNMO was published by Pasero in 2008.[12] The idea of oxygen defects in spinel materials, however goes back further and was already advocated for $LiMn_2O_4$ (LMO) cathode active materials.[13] Pasero found a reduced occupancy of the oxygen site of LNMO when refining neutron powder diffraction patterns of materials heated to temperatures above 650 °C under vacuum. These results, however, may not be representative for common LNMO materials calcined at ambient pressure and in oxygen containing atmospheres. Accordingly, in the same study, Pasero found full oxygen site occupancy in LNMO for a sample calcined in air. Since then, not a single neutron diffraction study found conclusive evidence for oxygen defects in LNMO spinel phases[10,11,14–16] even though a reduced site occupancy factors (s.o.f.) should be clearly evident, based on the high neutron scattering contribution of oxygen, and the fact that some very Mn(III) rich samples were investigated. To the best of our knowledge, there has never been any further direct proof of oxygen defects in the crystal structure of LNMO. A main experimental evidence for oxygen defects in LNMO, which is repeatedly cited, is thermogravimetric analysis (TGA).[10,12,13,17] The central weakness of this method, however, is that, although it is proven beyond doubt that the LNMO samples lose and absorb oxygen during heating and cooling, it is by no means proven that this oxygen loss is related to oxygen defects in the spinel phase.

An alternative explanation for Mn(III) in LNMO materials is advocated, for example, by the research groups of Dahn,[18] Cabana,[11] or Casas-Cabanas.[16] It is argued that the formation of the ubiquitous Ni-rich secondary phase, which Cabana identified as a Li containing rocksalt phase with a Ni:Mn ratio of 2:1,[11] has to be taken into account. The metal to oxygen ratio (M:O) in the rocksalt phase is 1:1 or close to it, while the spinel phase has a M:O ratio of 3:4. The rocksalt phase hence is nickel-rich and poor in oxygen compared to the LNMO phase. Thus, secondary phase formation leads to a Ni-loss in the spinel phase and oxygen loss during phase transformation, for example, according to:

$$LiNi_{0.5}Mn_{1.5}O_4 \rightleftharpoons n\ LiNi_{0.5-x}Mn_{1.5+x}O_4$$
$$+ m\ Li_y(Ni_{0.67}Mn_{0.33})_{1-y}O + k\ O_2 \quad (1)$$

The loss of Ni(II) has to be compensated by the reduction of Mn(IV) to Mn(III), according to $LiNi_{0.5-x}^{II}Mn_{1.5-x}^{IV}Mn_{2x}^{III}O_4$.[19] This consistently explains oxygen release, Mn(III) in LNMO and the formation of the secondary phase, without requiring oxygen defects in the spinel phase. Zhong and Dahn, who reported a comparable equation in 1997 noted that such reactions can be balanced,[18] which, however, was still pending for LNMO. Even before that, in 1993 Feltz published a detailed study with very similar findings on LNMO-related spinel phases $Li_zNiMn_{2-z}O_4$ ($0 \geq z \geq 2/3$).[20] The readership may have been limited due to the German language of the publication. Translation, however, is still worth the effort, as the impact of high temperature calcination on these spinel phases is discussed in detail. A secondary NiO-rocksalt phase is reported to form and a loss of Ni in the spinel phase

and oxygen release during the phase transition are described. In addition, a full and balanced reaction according to Equation (2) was presented anticipating the later findings on LNMO:

$$Li_zNiMn_{2-z}O_4 \rightleftharpoons \frac{3-n}{3}Li_{\frac{3z}{3-n}}Ni_{\frac{3-3n}{3-n}}Mn_{\frac{6-3z}{3-n}}O_4 + n\ NiO + \frac{n}{6}O_2 \quad (2)$$

But the work of Feltz addresses another important point. A basic dilemma for the synthesis of LNMO materials is, that the decomposition temperatures (often referred to as oxygen release temperatures[10]) are close to or above the temperatures required for crystal growth.[20] Feltz discussed this problem based on the examples of $Li_{0.66}NiMn_{1.33}O_4$ and $Li_{0.5}NiMn_{1.5}O_4$ in detail. It is noted, that a phase separation is inevitably coming along with the Equation (2) during high temperature treatment. It is argued that this phase separation is partly, but not fully reversible during cooling and further tempering steps. This finding is of outstanding importance for LNMO, since it yields a conclusive explanation why spinel phases like LNMO hardly can be obtained phase-pure at desired primary particle sizes in the μm range.

The fundamental work allowing for a more detailed understanding of the secondary phases in LNMO materials were published almost 10 years ago. In 2013, McCalla presented a comprehensive investigation on the Li–Ni–Mn–O system.[21,22] Besides the spinel phases, ordered rocksalt phases and Ni- and Mn-rich layered structures were observed. The studies illustrate that all crystal structures have a face centered cubic (fcc) packing of the oxygen anions in common and can therefore be transformed into each other by rearrangement of the cations, as shown in Figure S1, Supporting Information. In the spinel phase, 1/2 of the octahedral and 1/8 of the tetrahedral gaps are occupied by cations (M:O = 3:4), while in the rocksalt and layered phases, all octahedral positions are occupied (M:O = 1:1). Spinel phases are reported to be accessible up to a Ni:Mn ratio of 1:3. Compounds with higher Ni content, such as $Li_x(Ni_{0.5}Mn_{0.5})_{1-x}O$ crystallize as rocksalt ($Fm\overline{3}m$) or layered ($R\overline{3}m$) phases, depending on their Li content.[22–24] With Ni:Mn ratios of 2:1[11] or 6:1,[25] neutron diffraction studies indicate, that the LNMO secondary phases are Ni-rich, but not pure $Li_xNi_{1-x}O$ phases. While the latter crystallize as simple rocksalt phases (s-RS) with a small unit cell ($a \approx 415$ pm) in space group $Fm\overline{3}m$[24] the work of McCalla indicates that the quaternary rocksalt phases $Li_x(Ni_yMn_{1-y})_{1-x}O$ tend to form superstructures of the Mg_6MnO_8-type,[21] that is, "ordered" rocksalt phases (o-RS). With higher Li contents in the LNMO secondary phase, the cations again may separate into lithium and transition metal rich layers, which leads to a distortion along the cubic <111> direction resulting in a symmetry reduction of the side phase from space group $Fm\overline{3}m$ into the subgroup $R\overline{3}$m.[22,26] The relations of the unit cells are shown in Figure S1, Supporting Information, including (simplified) formulas for the unit cell transformation.

A persistent misconception in some studies on LNMO is the assumption that cation order and Mn(III) content are firmly linked to each other. We consider this assumption to be a reason for the customary categorization into "ordered" and "disordered" LNMO. As a result of typical calcining temperatures, "ordered LNMO," or "o-LNMO" usually refers to materials containing spinel phases close to ideal composition $LiNi_{0.5}Mn_{1.5}O_4$. "Disordered LNMO" or "d-LNMO," in contrast ubiquitously refers to samples with noticeable and varying amounts of Mn(III), and

thus Ni deficient spinel phases. Experimental evidence that cation order and Mn(III) content in LNMO are actually independent phenomena, however, were brought forward by Cai[14] and Aktekin[10] in 2013 and 2019, and confirmed in our previous study.[26]

The finding of the independence of both properties gave rise to the idea for this study, starting from the synthesis and investigation of atypical LNMO materials, namely materials containing Mn(III) rich ordered LNMO phases, and materials containing disordered spinel phases with low Mn(III) content. The investigation of these compounds allows to reassess critically the role of cation order for LNMO materials, but more importantly, in agreement with the studies mentioned above, it becomes obvious that there are systematic deviations between the spinel phase composition and the composition of the LNMO sample. Therefore unspecified use of the term "LNMO" for both, sample and spinel phase may lead to confusion. Within this study, we want to avoid ambiguity by using the terms "LNMO material" when referring to the sample and "LNMO phase" when referring to the spinel phase. It is shown that LNMO phase in hardly any material has the ideal composition $LiNi_{0.5}Mn_{1.5}O_4$. The assumption that oxygen defects according to $LiNi_{0.5}Mn_{1.5}O_{4-\delta}$ exist in the spinel phase seems convincing at first, as it can provide an easy explanation for the Mn(III) related redox activity of LNMO. However, from our point of view, this assumption has led to the current situation, where a thorough discussion of the actual phase and sample composition is still pending and we want to specifically address this issue. We provide multiple evidence contradicting oxygen defects and show that once this idea has been overcome, crystallographic and electrochemical properties to a large extend can be explained by the deviating Ni and Mn content in the spinel phase. This finally enables to establish, model, and understand fundamental relationships between compositions and crystal structures for the spinel and secondary phase, and to understand the resulting electrochemical properties of LNMO materials.

2. Experimental Section

2.1. Material Preparation

Pristine LNMO was prepared by a two-step spray drying synthesis. The starting compounds lithium acetate dihydrate ($LiOOCCH_3 \cdot 2H_2O$, 98%, Alfa Aesar), nickel acetate tetrahydrate ($C_4H_6NiO_4 \cdot 4H_2O$, ≥99.0%, Sigma Aldrich) and manganese acetate tetrahydrate ($C_4H_6MnO_4 \cdot 4H_2O$, ≥99.0%, Sigma Aldrich) were dissolved in distilled water. After complete dissolution, the aqueous solutions were mixed in stoichiometric ratios. Dried precursor powders were obtained by spray drying the precursor solutions. The precursor powders were then converted to the corresponding spinel oxide by a two-step calcination process in ambient atmosphere. In the first step, the precursors were calcined for 10 h at 500 °C. After cooling down to room temperature, a second calcination program at 800 °C (10 h) followed. Heating and cooling rates were 300 K h⁻¹. The obtained material was subsequently mixed with three equivalents of distilled water and ground for 24 h in a planetary ball mill (Fritsch Pulverisette 5, 3 mm ZrO_2 grinding balls) and then spray dried again. The obtained granules are hereafter referred to as pristine LNMO. The calcining programs yielding samples 1–4 are specified in **Table 1**. Before and after final calcination steps, the materials were passed through a sieve with a mesh width of 50 µm.

2.2. Material Characterization

The particle morphologies were studied by scanning electron microscopy (SEM) with a Zeiss Supra 55 FE-SEM using an acceleration voltage of 4–5 kV. The LNMO granule powders were fixed on carbon adhesive tape.

Nitrogen physical adsorption isotherms were measured with a surface area analyzer Gemini VII 2390 (Micromeritics). Calculations of the specific surface were performed according to the Brunauer–Emmett–Teller (BET) theory. From each sample about 0.8 g was used for analysis. Prior to the measurements, the specimens and tubes were dried under vacuum at 120 °C.

Raman spectra were collected at room temperature with a Horiba Jobin-Yvon LabRAM HR spectrometer equipped with an Olympus microscope BXFM. A HeNe-laser with a wavelength of 633 nm was used as an excitation source. The spectra were collected from single granule particles by scanning surface areas of 4×4 µm in a range from 100 to 800 cm⁻¹.

The crystal structures of the LNMO and the secondary phases were investigated by means of powder X-ray diffraction (PXRD). The room temperature measurements were carried out on an advanced laboratory diffractometer (Typ 5021, Huber) equipped with a microfocus rotating anode X-ray generator (Rigaku MM007, Mo-K_α radiation, parallel collimated beam, Ø ≈ 2 mm) and a 2D Pilatus 300K-W detector, with a sample to detector distance of 0.7 m.[27] Measurements were carried out in an angular range of $7° < 2\theta < 47°$. In order to reliably track small changes in the lattice parameter, all samples, together with a standard reference material (LaB_6 NIST SRM 660c) were

Table 1. Details on the calcination of the LNMO materials. The prefixes o- and d- stand for ordered and disordered. The numbers 49–43 represent the Ni-content of the LNMO phases. The labeling is explained in detail in Section 4.1. The reason for using different calcination atmospheres is explained in Section 3.2.

	Sample	Starting material	Thermal treatment and atmosphere	
1	o-LNMO-49	pristine	RT $\xrightarrow{600\,K\,h^{-1}}$ 900 °C (10 h) $\xrightarrow{600\,K\,h^{-1}}$ 680 °C (20 h) $\xrightarrow{10\,K\,h^{-1}}$ 350 °C $\xrightarrow{100\,K\,h^{-1}}$ RT	air
2	d-LNMO-48	o-LNMO-49	RT $\xrightarrow{600\,K\,h^{-1}}$ 750 °C (0.5 h) $\xrightarrow{600\,K\,h^{-1}}$ 550 °C $\xrightarrow{10\,K\,h^{-1}}$ 450 °C $\xrightarrow{100\,K\,h^{-1}}$ RT	air
3	d-LNMO-44	pristine	RT $\xrightarrow{600\,K\,h^{-1}}$ 900 °C (10 h) $\xrightarrow{600\,K\,h^{-1}}$ RT	air
4	o-LNMO-43	d-LNMO-44	RT $\xrightarrow{600\,K\,h^{-1}}$ 600 °C (18 h) $\xrightarrow{600\,K\,h^{-1}}$ RT	Ar

Table 2. Detailed information on the LNMO cell tests. All currents refer to the theoretical capacity of 146.8 mAh g^{-1}. After cell formation and standard cycling (Steps 1 and 2), a rate capability test was performed (Steps 3 to 7). Cycling stability was then tested over 200 cycles (Step 8). Step 5 consists of two control cycles that are not actually part of the rate test.

Step	Cycles	First cycle #	Last cycle #	Charge rate [C]	Discharge rate [C]
1	2	1	2	0.05	0.05
2	10	3	12	0.5	0.5
3	4	13	16	0.5	1.0
4	4	17	20	0.5	2
5	2	21	22	0.5	0.5
6	4	23	26	0.5	5
7	4	27	31	0.5	10
8	200	32	231	0.5	0.5

packed separated from each other, into a single glass capillary with a diameter of 0.5 mm. Subsequently, a serial measurement was carried out by translating the capillary position along the capillary rotation axis. The capillary setup was optimized to track small changes within a series of crystalline materials while excluding common sources of error, such as sample displacement or temperature fluctuations.[28] The crystal structures were refined by the Rietveld method[29] using the TOPAS 6 software. It was well known that the estimated standard deviations (e.s.d.) obtained by this method tend to underestimate the actual error range.[30] According to Bérar[31] the e.s.d. were multiplied with a factor of 5 in order to obtain the estimated probable errors (e.p.e.) which are specified hereafter.

In addition pristine LNMO was investigated by means of in situ high temperature X-ray diffraction on a Bragg–Brentano Diffractometer (D8 Advance, Bruker) equipped with a heating chamber (HTK1200N, Anton Paar), a Cu-K_α X-ray tube and a silicon strip detector. The pristine LNMO material was loaded on a corundum crucible and put the heating chamber at ambient atmosphere. A total of 30 measurements were carried out in the range of $15° < 2\theta < 74°$, with a step width of 0.02° and step time of 0.333 s per step, that is, the recording time for each pattern was about 20 min. Heating and cooling rates of 600 K h^{-1} were applied. During the measurements, temperatures were kept constant. Serial Rietveld refinements were applied to refine the lattice parameters and phase fractions of LNMO and the secondary phase. A uniform isotropic displacement parameter $B = 0.5$ was used for all atomic positions and temperatures. Profile broadenings were modeled using common parameters for crystal size and strain broadening for both phases. According to Bérar,[31] the e.s.d. were multiplied with the factor of 3 in order to obtain the estimated probable errors (e.p.e.) which are specified hereafter.
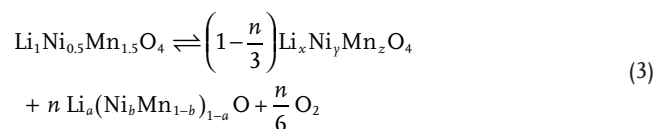
For electrochemical characterization, slurries were prepared by mixing the additives carbon black (Super C65, Timical/Imerys) and polyvinylidene fluoride (PVDF, Solef 5130, Solvay) with 1-methyl-2-pyrrolidinone (NMP) with a dissolver stirrer. Then the LNMO active materials were added and the final slurries were obtained by mixing the components with a Speed-Mixer DAC 150 (Hausschild) for at least 5 min at 2000 rpm. In the next step, the slurries were coated on Al foil with a 200 mm notch bar spreader and dried in air at 80 °C for at least 1 h

before being transferred to a 110 °C vacuum chamber, where the drying process was continued for at least 16 h. With final cathode compositions of 80/10/10 for LNMO, carbon black and PVDF, active material loadings of 3.8 to 4.2 mg cm^{-2} were obtained. Before cell assembly, cathodes of 15 mm in diameter were compressed by a hydraulic press with a force of 4 kN and once again dried for at least 1 h in a vacuum oven at 110 °C. CR2032 coin cells made of SUS316L stainless steel were then assembled in an argon filled glovebox with lithium foil as the anode. A stack of three separators (Cellgard 2325, Whatman GF/C, Cellgard 2325) and 200 µL LP30 electrolyte (1.0 M LiPF$_6$ solution in 1:1 v/v ethylene carbonate:dimethyl carbonate) were used. Electrochemical measurements were carried out on a LBT20084 battery tester (Arbin Instruments) by galvanostatic charge/discharge cycling in the voltage range of 3.5 to 5 V. Rate capability and cycling stability tests were combined. The detailed testing procedure is listed in **Table 2**. From each materials four coin cells were built. For representative results of the rate capability and cycling stability tests, the results of the worst cell was omitted and the average capacity of the three best cells was calculated, together with the standard deviation.

3. Results

3.1. Theoretical Composition of LNMO Materials

In the synthesis process LNMO precursor materials usually yielding the stoichiometric LNMO composition LiNi$_{0.5}$Mn$_{1.5}$O$_4$, are calcined to obtain spinel type LNMO materials. As discussed before, this process is accompanied by the formation of a secondary phase and the release of oxygen,[11,20] according to Equations (1) or (2). As this reaction is not fully reversible due to phase separation, even for slow cooling rates and prolonged tempering steps, secondary phase residuals remain.[20] Due to the different M:O ratios of the LNMO and the secondary phase, the overall oxygen loss is proportional to the remaining secondary phase fraction. Following the basic principles of stoichiometry and three simple assumptions: a) the M:O ratio in the spinel phase is 3:4, b) the M:O ratio in the secondary phase is 1:1, and c) the secondary phase can contain different Li contents and different Ni:Mn ratios, a general formula for the LNMO synthesis can be established according to:

$$\text{Li}_1\text{Ni}_{0.5}\text{Mn}_{1.5}\text{O}_4 \rightleftharpoons \left(1-\frac{n}{3}\right)\text{Li}_x\text{Ni}_y\text{Mn}_z\text{O}_4 + n\,\text{Li}_a(\text{Ni}_b\text{Mn}_{1-b})_{1-a}\text{O} + \frac{n}{6}\text{O}_2 \tag{3}$$

For the secondary phase, a defines the Li content and via the parameters b, the Ni- and Mn-content can be specified. The phase fraction of the spinel phase, the secondary phase fraction and the oxygen release are determined by the turnover parameter n. The resulting LNMO phase composition is described by the parameters x, y, and z. These parameters are calculated according to Equations (4) to (6).

$$x = \frac{1-a\,n}{1-\frac{n}{3}} \tag{4}$$

$$y = \frac{0.5 - [n\,b\,(1-a)]}{1 - \frac{n}{3}} \quad (5)$$

$$z = \frac{1.5 - [n\,(1-b)\,(1-a)]}{1 - \frac{n}{3}} \quad (6)$$

The formulas can be adapted for different starting material compositions, yielding Equations (S1)–(S4), which are listed in the Supporting Information. However, for varying the starting composition, the stability ranges of the spinel phase[21,22] should be kept in mind. The practical application and relevance of Equations (3)–(6) is discussed in Section 4.9.

3.2. Different Types of LNMO Materials

Apart from the chemical composition, LNMO materials may vary with regard to cation order in the spinel phase. Accordingly, we were able to synthesize four different types of LNMO materials, which are listed in **Table 3**. Sample 1 (o-LNMO-49) represents what would commonly be referred to as an "ordered LNMO" material. It has a close to stoichiometric spinel composition $LiNi_{0.49}Mn_{1.51}O_4$ and high degree of cation ordering. Sample 2 (d-LNMO-48) was obtained by shortly heating a part of sample 1 to 750 °C, which is above the order-to-disorder transition temperature ($T_{O \to D}$). Thus a disordered LNMO phase with a low proportion of Mn(III) was formed, which, to the best of our knowledge, has not been prepared before. Sample 3 (d-LNMO-44) again corresponds to what would commonly be referred to as standard "disordered LNMO" with an approximate main phase composition $LiNi_{0.44}Mn_{1.56}O_4$, and hence significant Mn(III) content. Sample 4 (o-LNMO-43) was obtained by calcining a part of sample 3 under an argon atmosphere at 600 °C for 18 h. While this temperature allows for the formation of cation ordering in the LNMO crystal structure, the Ar atmosphere prevents oxygen uptake and the rocksalt to spinel phase transition. Therefore a similarly high Mn(III) content as in sample 3 is obtained. Hence, the main phase of sample 4 is a Mn(III)-rich (partially) ordered LNMO phase. Details on the determination of the composition and cation order are discussed below. However, the sheer existence of four different types of LNMO phases shows, that the classification into "ordered" and "disordered" LNMO is insufficient. We therefore use an extended classification of LNMO materials based on the Ni-content of the spinel phase. A detailed discussion is given in Section 4.1.
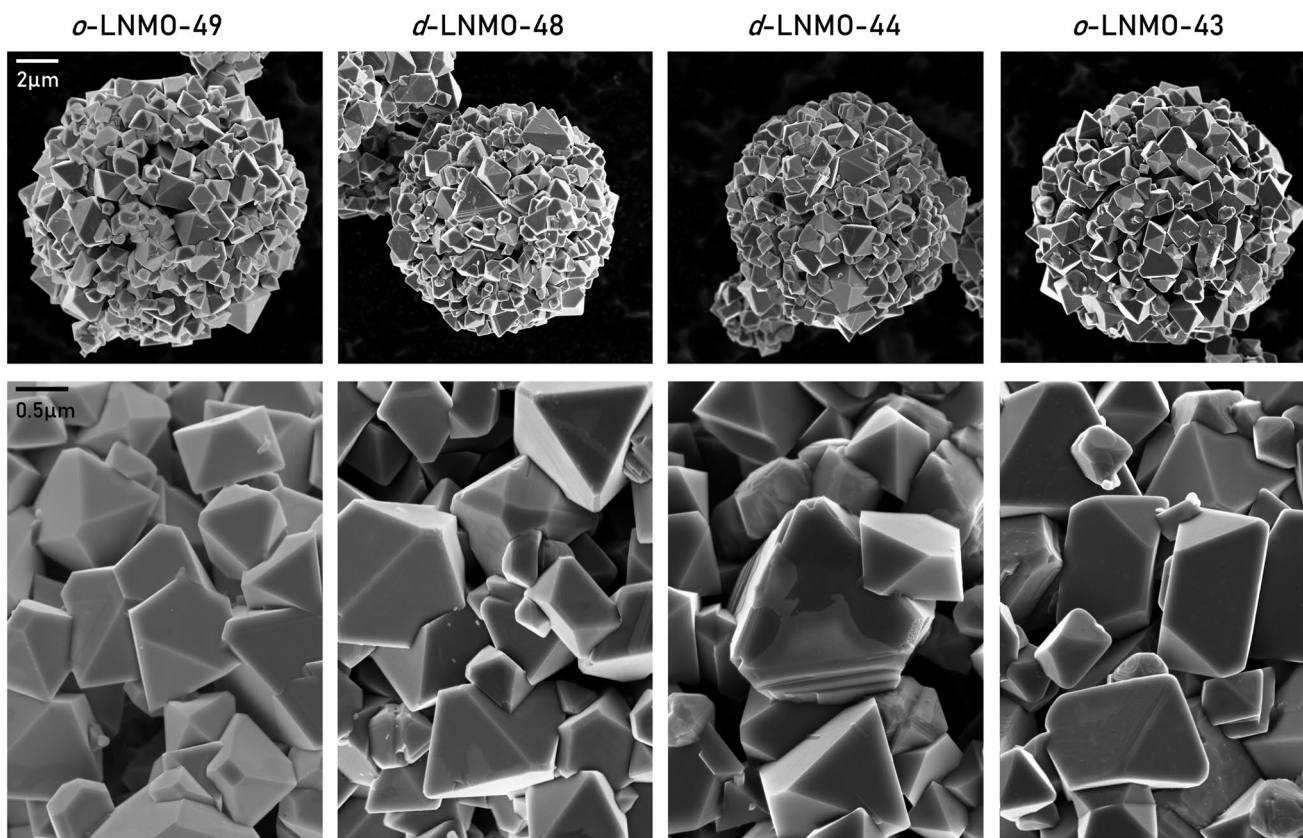
3.3. Particle Morphology

A common problem when studying LNMO materials is that the electrochemical characteristics are determined by both morphological and chemical properties. In order to exclusively investigate the effect of the spinel phase crystal chemistry on the material properties, it is therefore crucial to minimize variations of the morphology, such as primary crystal size and shape or the specific surface area.[32,33] In a previous study[26] it was shown how uniform morphologies for different calcination temperatures and cooling rates can be achieved through multi-stage calcination programs. The same approach is pursued in the present work. SEM images of the samples 1 to 4 are shown in **Figure 1**. All LNMO materials consist of porous spherical granules with uniform secondary particle size distributions. The average size of the granules is around 10 µm for all samples, with individual diameters ranging from roughly 5 to 15 µm. As listed in Table 3, the specific surface areas of the materials are very close to each other with values between 1.0 and 1.2 m² g⁻¹. Based on a mercury intrusion porosimetry experiment conducted on an analogously prepared LNMO material with a specific surface area of 1.2 m² g⁻¹, a porosity of approximately 34% is expected for all samples.

The SEM images also confirm that primary particle sizes and size distributions for samples 1 to 4 hardly differ. The octahedral LNMO phase primary particles have edge lengths of roughly 0.4 to 2 µm. In good agreement with the Rietveld refinements (see below), increased secondary phase fractions are visible in samples 3 and 4. The granules samples show extended surface regions which appear brighter in the SEM images. As already confirmed by energy-dispersive X-ray spectroscopy,[26,34] these areas can be attributed to secondary phases, which have a higher density due to the higher M:O ratio of 1:1 compared to 3:4 for the LNMO phase (rocksalt $Li_{0.3}Ni_{0.2}Mn_{0.5}O$ $\rho = 5.4$ g cm⁻³[22] versus spinel $LiNi_{0.5}Mn_{1.5}O_4$ $\rho = 4.45$ g cm⁻³[15]). The octahedral LNMO primary particles of sample 4 show additional damage. The edges and corners are rounded, which indicates partial LNMO decomposition during the 18 h treatment at 600 °C in argon. It also seems conceivable that these LNMO particles have a closed secondary phase layer on the surface. When the SEM images were acquired, sample 1 (o-LNMO-49) showed a comparatively strong electrostatic charging and less brightness and contrast, which can be seen as an indication of reduced electronic conductivity of the fully lithiated state.[35]

3.4. Raman Spectroscopy

Raman spectroscopy is a sensitive method to probe the local symmetry of the transition metal ions in LNMO materials, and therefore to determine whether the spinel phase has a predominantly ordered ($P4_332$) or disordered ($Fd\bar{3}m$) crystal structure. The Raman spectra of samples 1–4 are shown in **Figure 2** and allow for a qualitative classification of the LNMO phases as ordered, partially ordered, or disordered. All spectra were

Table 3. General properties of the synthesized LNMO materials. Samples 2 and 4 represent uncommon types of LNMO materials, which have been rarely or never investigated before.

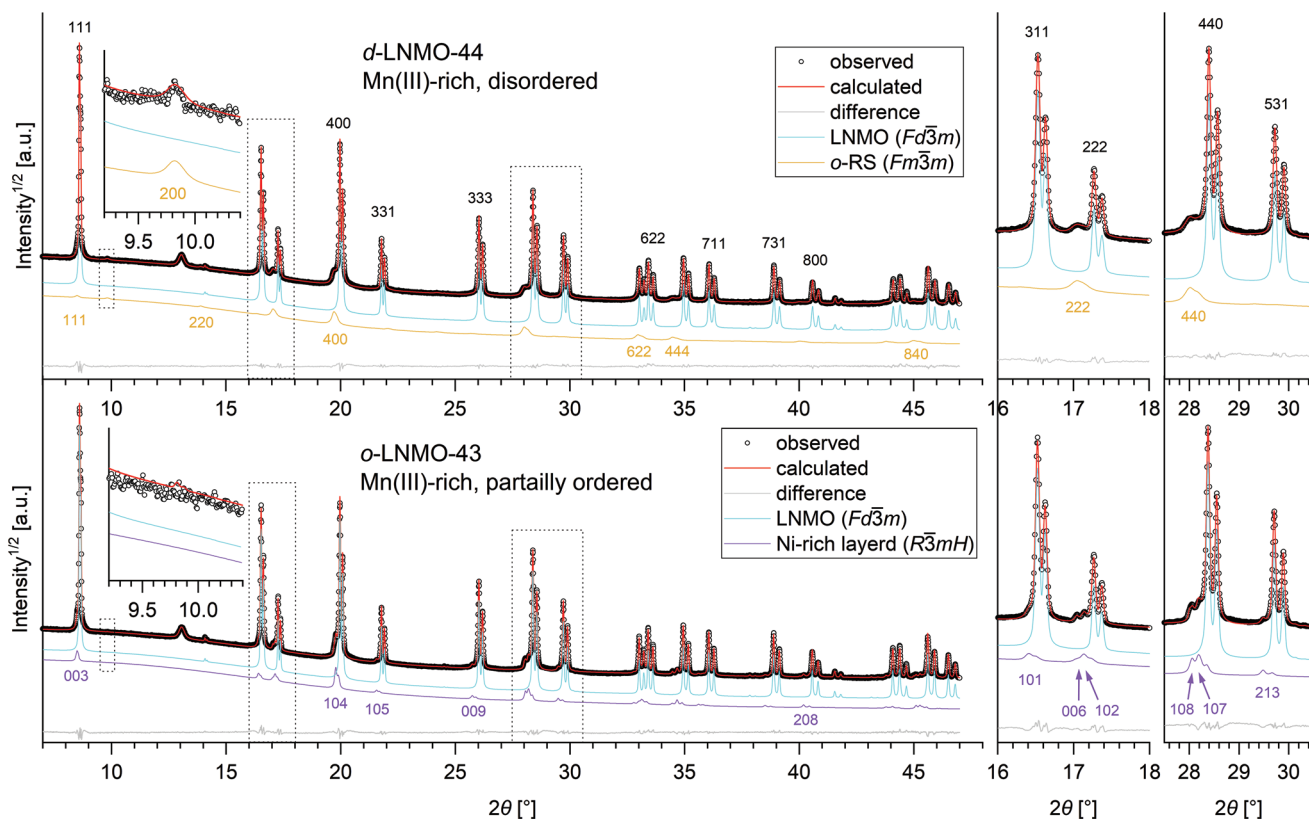|	Sample	Mn(III)-content	Spinel phase cation order	Specific surface area (BET)
1	o-LNMO-49	Mn(III)-poor	ordered	1.0(1) m² g⁻¹
2	d-LNMO-48	Mn(III)-poor	disordered	1.2(1) m² g⁻¹
3	d-LNMO-44	Mn(III)-rich	disordered	1.0(1) m² g⁻¹
4	o-LNMO-43	Mn(III)-rich	(partially) ordered	1.1(1) m² g⁻¹

Figure 1. SEM images of the different LNMO materials. The aim was to achieve a uniform particle morphology for all specimens. Cation ordering and Mn(III) content deliberately vary. From the left to right side, the secondary phase fraction increases and the Ni content in the LNMO phase decreases.
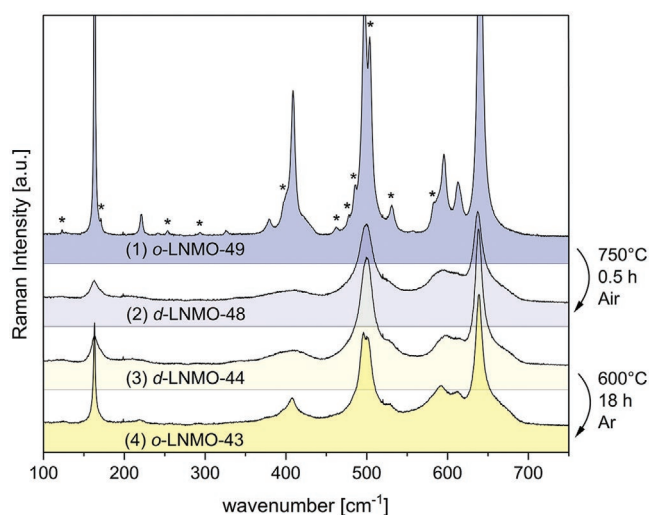
Figure 2. Raman spectra of the four types of LNMO materials. Samples 1 and 2 (blue) have a low Mn(III) content, samples 3 and 4 (yellow) are rich in Mn(III). The spectra of samples 2 and 3 displayed with pale colors suggest a disordered LNMO crystal structure, while those of samples 1 and 4 indicate ordered and partially ordered structures. To the best of our knowledge, Raman modes marked with an asterisk have not yet been observed before.

collected with identical measurement parameters. Samples 2 and 3 (d-LNMO-48 and d-LNMO-44) show very similar spectra, which are fully consistent with the commonly specified properties of disordered LNMO.[36,37] The Raman spectra of sample 4 (o-LNMO-43) in contrast, provides typical features of ordered LNMO. In comparison to the disordered phases, T_{2g} and E_g modes at 160 and 410 cm^{-1} exhibit higher intensities, and the A_{1g} modes of Mn^{4+} and Ni^{2+} at 590 and 610 cm^{-1} can clearly be distinguished. The minor features at 218 and 240 cm^{-1} characteristic for ordered materials,[37] however, are rather weak. As an additional feature, the splitting of the band around 495 cm^{-1} is observed. This, to the best of our knowledge, has not been reported before and might be due to slightly deviating energies of A_1 and E modes, which were predicted to occur around this wavenumber.[38] The Raman spectrum of sample 1 (o-LNMO-49) likewise indicates cation order. However, notably sharper peaks are observed. The spectrum reveals a total of 11 additional modes which have not been observed in previous studies, and which suggests that this LNMO phase might have the highest degree of cation ordering reported so far. A high resolved representation of the spectrum is shown in Figure S2, Supporting Information. For all newly observed Raman bands, suitable modes were predicted as a result of density functional theory (DFT) calculations by Miwa[38] and suggestions for the band assignment are listed in the Supporting Information.

**ADVANCED
SCIENCE NEWS**

www.advancedsciencenews.com

**ADVANCED
ENERGY
MATERIALS**

www.advenergymat.de

Figure 3. Rietveld refinement of the Mn(III) rich disordered and partially ordered LNMO materials *d*-LNMO-44 (top) and *o*-LNMO-43 (bottom). The individual contributions of the LNMO (cyan), ordered rocksalt (gold) or Ni-rich layered phases (purple) are set off vertically. Some 2θ ranges of special interest for the determination of the crystal structures of the secondary phases are highlighted. The broad reflections at 13° originate from the glass capillary.

A further remarkable feature of *o*-LNMO-49 is that the Raman intensity is significantly higher compared to all other spectra. A conclusive explanation, was given by Kunduraci et al.[39] who attributed this observation to the reduced intrinsic electronic conductivity of samples containing Mn(IV) almost exclusively. It is suggested, that the low conductivity allows for an increasing penetration depth of the exciting photons, and thus for a stronger Raman effect. However, regarding this, it has to be noted that the reduced electronic conductivity is a peculiarity of the fully lithiated state and not an intrinsic property of ordered or close to stoichiometric LNMO phases.[35]

Regardless of the uncertainties in Raman band assignment and intensities, the spectra undoubtedly show that *o*-LNMO-49 has a highly ordered crystal structure and that a short temperature treatment at 750 °C yields a spinel phase with disordered structure (*d*-LNMO-48). The Mn(III) rich *d*-LNMO-44, which in contrast initially has a disordered crystal structure, can be transformed into a partially ordered phase by calcining at 600 °C in an argon atmosphere. The high Mn(III) content in *o*-LNMO-43 most likely prevents the formation of a higher degree of cation order, as discussed in Section 4.4.

3.5. Powder X-Ray Diffraction

The room temperature PXRD diffraction patterns of the Mn(III) rich samples *d*-LNMO-44 and *o*-LNMO-43 together

with the corresponding Rietveld refinements are shown in **Figure 3**. The refinements of *o*-LNMO-49 and *d*-LNMO-48 are depicted in Figure S3, Supporting Information. All LNMO phases were refined using a structure model of fully disordered $LiNi_{0.5}Mn_{1.5}O_4$ based on the $MgAl_2O_4$ structure-type. Despite a careful inspection, super structure reflections originating from cation ordering were not observed in the diffraction patterns. Reflections originating from secondary phases, in contrast, were found ubiquitously. Profile parameters were refined independently for each phase. As reported in a previous study,[26] additional reflections were observed, indicating that the description as simple rocksalt phase (*s*-RS, NaCl structure type, a ≈415 pm) is insufficient. As listed in **Table 4**, for samples 1–3 the secondary phase reflections could be refined using a model of an ordered rocksalt phase (*o*-RS, Mg_6MnO_8-type, refined as $Li_{0.3}Mn_{0.2}Ni_{0.5}O$[22]) yielding a lattice parameter around 829 pm. Based solely on this lattice parameter, a suitable quaternary phase compositions could be, for example, $Li_{0.25}Ni_{0.65}Mn_{0.1}O$.[21]

In the diffraction pattern of *o*-LNMO-43, the 200 reflection of *o*-RS at 10° is no longer observed and splitting of the 440 reflection at 28° indicates a symmetry reduction to a rhombohedral phase (cf. Figure 3). The secondary phase therefore could be properly refined using a structure model of the α-NaFeO$_2$ structure-type (refined as $Li_{0.4}Ni_{0.6}O$, structure model from ref. [24]). The lattice parameters were refined to $a = 291.3$ and $c = 1436.5$ pm, which roughly correspond to those of a Ni-rich layered phase $Li_{0.46}Mn_{0.378}Ni_{0.754}O_{1.863}$ described by McCalla

ADVANCED
SCIENCE NEWS
www.advancedsciencenews.com

ADVANCED
ENERGY
MATERIALS
www.advenergymat.de

Table 4. Results of the Rietveld refinements. Errors stated are estimated probable errors.

	Sample	LNMO ($Fd\overline{3}m$)		o-RS ($Fm\overline{3}m$)		Ni-rich layered ($R\overline{3}mH$)			R(wp)
		a [pm]	[wt%]	a [pm]	[wt%]	a [pm]	c [pm]	[wt%]	[%]
1	o-LNMO-49	816.941(9)	98.8(1)	831.6(2)	1.2(3)				3.0
2	d-LNMO-48	817.170(9)	97.6(2)	829.6(2)	2.4(4)				2.7
3	d-LNMO-44	817.929(12)	94.3(2)	829.0(2)	5.7(3)				2.7
4	o-LNMO-43	818.350(2)	91.6(2)	829.0a)	0.4(1)	291.30(2)	1436.48(2)	8.0(2)	2.9

a)Indicates constrained parameters.

(a = 291.6 pm, c = 1432.4 pm).[22] However, both lithium and oxygen content most likely deviate somewhat due to rather different thermal treatments. Interestingly, the secondary phase compositions estimated based on the studies of McCalla have Ni:Mn ratios around 2:1 and 6.5:1 and thus show close similarities to the Ni:Mn ratios found by Cabana (2:1)[11] and Kiziltas–Yavuz (6:1).[25]

In **Figure 4**a, the lattice parameters of the LNMO phases based on their Ni-content are shown. The latter was taken from the voltage profile evaluation of the samples (see below). The lattice parameter of the spinel phase decreases with increasing
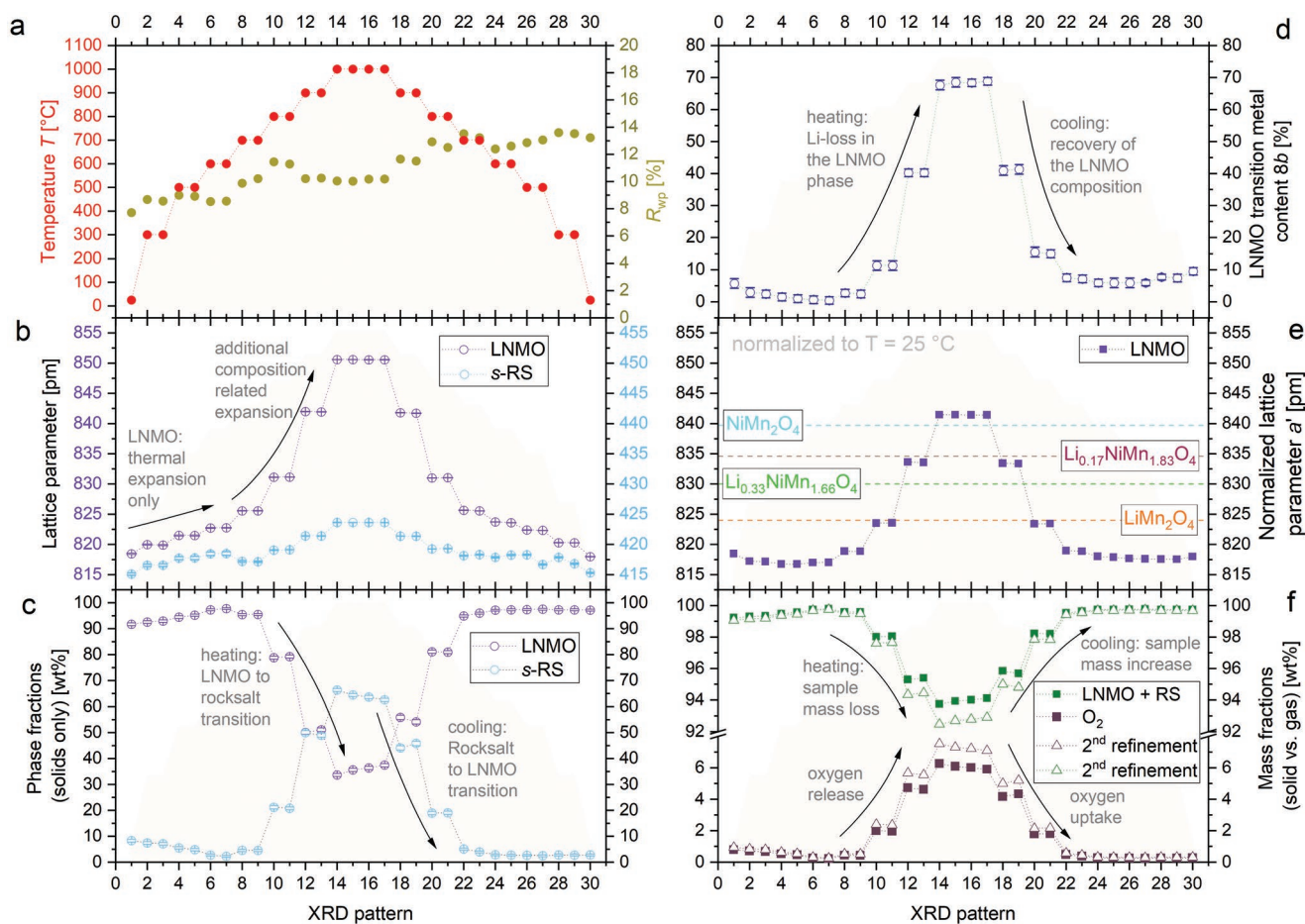
Ni-content. This behavior is well known from previous studies and the data on $LiNi_xMn_{2-x}O_4$ (0 ≥ x ≥ 0.5) provided by Zhong suggests Vegard behavior.[18] A corresponding fit based solely on the a-values of the samples 1–3 which were calcined in air, yields very consistent results: the extrapolation of the lattice parameter to x = 0, that is, to $LiMn_2O_4$, yields a lattice parameter of a = 825.3(3) pm. This is somewhat larger compared to the value reported by Zhong ($LiMn_2O_4$: a = 824.3 pm)[18] but in good agreement with other experimental findings (e.g., Berg, $LiMn_2O_4$: a = 825.1 pm).[40] Figure 4a thus confirms, that the Ni-content of the spinel phase, is very well suited to classify of LNMO materials, but more importantly, it is confirmed, that the Ni values derived from the voltage profiles precisely yield the expected linear relationship between Ni content of the LNMO phase and lattice parameter. Figure 4b shows a plot of the phase fractions of samples 1–4 against the Ni-content in the LNMO phase. In agreement with Equations (3)–(6) it becomes obvious, that for a uniform starting material composition, decreasing Ni content in the spinel phase is linked to increasing secondary phase fractions. The plot also demonstrates that the experimental phase fractions are in good agreement with phase fractions calculated as a function of the Ni content in the LNMO phase (see below).

3.6. High Temperature PXRD

An in situ high temperature study was conducted to provide some data for a better understanding of the calcining processes of LNMO materials and in order to quantify the phase fraction of the secondary phase at high temperatures. From the latter, the oxygen release/uptake of the LNMO sample can be calculated for each temperature. Due to the fast acquisition, the patterns do not allow for a detailed analysis of structural properties of the secondary phases as above. In order to obtain a robust refinement, a s-RS model of the secondary phase with the composition $Li_{0.33}Ni_{0.44}Mn_{0.22}O$ was applied, and profile parameters of both phases were coupled. LNMO initially was refined as $LiNi_{0.5}Mn_{1.5}O_4$, starting from the $Fd\overline{3}m$ structure model mentioned above. As shown in Figure S4, Supporting Information, at 800, 900, and 1000 °C, increased intensities of the 002 and 422 reflections of the LNMO phase were observed, which indicate a partial occupation of the 8b tetrahedral position with transition metal ions.[41] Due to the similar structure factors of Mn and Ni, the refinement of the XRD patterns does not allow to distinguish between Ni and Mn on the 8b site. Therefore, during the refinement process, a simplified structure model

Figure 4. Results of the Rietveld refinement. a) Lattice parameter of the spinel phase versus the Ni-content derived from the voltage profiles. b) Phase fractions of the LNMO and the secondary phase. In the shown Ni-range, the oxygen related mass loss is expected to be ≤0.55 wt% and was therefore neglected. The lines correspond to a calculation of the phase fractions based on Equations (3)–(6) for a secondary phase composition of $Li_{0.33}Ni_{0.44}Mn_{0.22}O$ (cf. Section 4.9).

Figure 5. a–d) Results of the Rietveld refinements of the in situ high temperature XRD study: Measurement temperature and resulting R_{wp} value (a); Lattice parameters for LNMO and the secondary phase (b); Phase fractions obtained from the refinements (c). Transition metal content ω on Wyckoff site 8*b* (d). Further evaluation of the Rietveld results: e) Composition related increase of the lattice parameter, obtained after the subtraction of the thermal expansion and compared to the lattice parameters of different spinel phases.[18,20,40] f) Calculation of the mass fractions of the solids (LNMO + rocksalt) versus the gas phase (O_2), calculated based on Equations (3)–(7). Secondary phase compositions $Li_{0.33}Ni_{0.44}Mn_{0.22}O$ (squares) and $Li_{0.5}Ni_{0.4}Mn_{0.1}O$ (triangles) were assumed.

with a site mixing parameter ω was used, allowing for the partial substitution of Li by Mn on Wyckoff site 8*b* according to $Li_{1-\omega}Mn_\omega Ni_{0.5}Mn_{1.5}O_4$.

For each temperature step, a XRD pattern with the corresponding Rietveld refinements is shown in Figure S4, Supporting Information. The reflection profiles of the first five patterns are uniformly broad, presumably due to a crystallite size effect resulting from the extensive ball milling prior to the final spray drying process. This changes with temperatures reaching 700 °C, where a sharpening of the reflections can be seen, indicating the onset of primary particle growth. From pattern number 8 onward, the diffraction patterns of the same temperature steps hardly differ from each other, which indicate that the system quite quickly gets into an equilibrium state at temperatures of 700 °C and above. Key results of the refinements for all 30 patterns are shown in **Figure 5**. Figure 5a reflects the temperature profile of the experiment, which includes heating to 1000 °C and cooling back to room temperature. The resulting lattice parameters of the LNMO and secondary phase as well as the corresponding phase fractions are shown in Figure 5b,c and

are in good agreement with the values reported previously.[14] A minimum of the secondary phase fraction is observed for the patterns measured at 600 °C. From 800 °C and above, the secondary phase fraction increases considerably to roughly 20, 50, and 65 wt% at 800, 900, and 1000 °C, which indicates increasing reaction turnover parameters n in Equation (3). Similar results for the formation of the secondary phase as a function of calcination temperature have been reported by Cai.[14] The lattice parameter of the LNMO phase increases drastically at temperatures of 800 °C and above. As shown in Figure 5d, the value of the refined site mixing parameter increases accordingly. The tetrahedral positions are occupied by transition metal ions by roughly 15%, 40%, and 70% at 800, 900, and 1000 °C. These values, however might be somewhat error prone, as the phase compositions might significantly deviate from the compositions of the refinement models and because of a strong peak overlap of the two phases.

For temperatures up to 600 °C the lattice parameter increase of the LNMO phase suggests a close to linear expansion of the unit cell with the temperature. From the refinement results of

ADVANCED
SCIENCE NEWS

www.advancedsciencenews.com

ADVANCED
ENERGY
MATERIALS

www.advenergymat.de

the XRD patterns 24–30, the volumetric thermal expansion of the LNMO phase was estimated to be 20.2×10^3 pm^3 K^{-1}. Based on this expansion coefficient, the normalized lattice parameters a' for $T = 25$ °C were calculated and are shown in Figure 5e. It becomes obvious, that for temperatures between 800 and 1000 °C the increase of a' is, far beyond the scope of thermal expansion. The a' values calculated, indicate a significant loss of lithium from the spinel phase during high temperature stages, as there are no known Li(Ni,Mn)$_2$O$_4$ phases with sufficiently large lattice parameters. For instance, for LiMn$_2$O$_4$, only about 824 to 825 pm are expected.[18,40] In good agreement with the previously presumed Li loss and transition metal occupation of the tetrahedral positions in the spinel structure, intermediate phases with reduced lithium to transition metal (Li:TM) ratios and suitable lattice parameters have been reported, like, for example, Li$_{0.33}$NiMn$_{1.66}$O$_4$ ($a = 830.0$ pm) and Li$_{0.17}$NiMn$_{1.83}$O$_4$ ($a = 836.6$ pm).[20] The normalized lattice parameter of the spinel phase calculated for 1000 °C is 841 pm, which close to the value expected for pure NiMn$_2$O$_4$ ($a = 839.7$ pm).[20] This composition, is not fully consistent with transition metal occupation parameter still yielding 30% Li occupation on the 8b site. Nevertheless, it becomes evident from the refinements, that at high temperatures the spinel phase loses significant amounts of Li, which inevitably leads to secondary phases with an increased Li-content.

The different M:O ratios of 1:1 for the spinel phase and 3:4 for the secondary phase, lead to the release or uptake of oxygen, according to $n(\text{O}_2) = 1/6\, n(\text{RS})$ (cf. Equations (2) or (3)). Hence based on the mass of the secondary phase, the mass of oxygen released is

$$m\left(\text{O}_2\right) = m\left(\text{RS}\right) \times \frac{M\left(\text{O}_2\right)}{6\, M\left(\text{RS}\right)} \quad (7)$$

With 56.7 g mol^{-1} for Li$_{0.33}$Ni$_{0.44}$Mn$_{0.22}$O, the mass of oxygen results as $m(\text{O}_2) \approx m(\text{RS}) \times 0.094$. The overall mass fraction of the solid phases and oxygen were calculated and the results are shown in Figure 5f. A reduction of the specimen mass by roughly 2, 4, and 6 wt% is expected to occur at 800, 900, and 1000 °C. The Rietveld refinements were repeated with an adapted composition for the rocksalt phase (Li$_{0.5}$Ni$_{0.4}$Mn$_{0.1}$O). This variation did not notably affect the LNMO phase and likewise converged very well, yielding similar R_{wp}-values compared to the initial run. Based on the reduced molar mass of this secondary phase ($M = 48.4$ g mol^{-1}), the mass of oxygen is $m(\text{O2}) \approx m(\text{RS}) \times 0.110$. This results in slightly higher values for the mass loss of the specimen by roughly 2, 5, and 7 wt% for 800, 900, and 1000 °C (triangles in Figure 5f). A discussion of these values is given in Section 4.8.

3.7. Electrochemical Characterization

The voltage profiles during the second cycle (0.05 C) of the tested cells (four cells for each synthesized material) are shown in **Figure 6**a. For each LNMO material, the four cells yield very similar results, with nearly identical voltages and only minor deviations with regard to the total capacity. The specific discharge capacities of the LNMO materials, calculated

as the mean value of all four individual cells are 138.2(6) and 138.9(8) mAh g^{-1} for o-LNMO-49 and d-LNMO-48. The discharge capacities are significantly reduced for the Mn(III) rich samples 3 and 4 (132.5(3) and 125.2(6) mAh g^{-1}), which can be conclusively explained by the increasing phase fractions of the electrochemically inactive secondary phase. It becomes obvious, that samples 1 and 2 have weakly pronounced Mn$^{4+/3+}$ steps indicating low Mn(III) content. For samples 3 and 4 more pronounced Mn$^{4+/3+}$ steps are observed, just like for most "disordered LNMO" materials discussed in literature. However, as stated before,[33] we want to emphasize, that the degree of cation order by no means can be determined based on these different Mn$^{4+/3+}$ related redox contributions, but is only reflected in the voltage of the Ni$^{2+/3+}$ plateau (see below).

The capacity variation of the individual cells is probably due to minor errors in the determination of the cathode active material loading and can be omitted by normalizing the capacity. The corresponding normalized discharge profiles for all investigated cells are shown in Figure 6b and reveal a high degree of consistency. The individual voltage contributions taken from these discharge profiles are listed in **Table 5**. As discussed in Section 4.2, the compositions of the individual LNMO phases can be determined very reliably based on these voltage profiles, which lead to the compositions stated in Table 5.

As reported by Song,[17] cation ordering influences the voltage of the redox plateaus of nickel, or, more precisely, on the voltage of the Ni$^{3+/2+}$ plateau. This effect is difficult to see in the voltage versus capacity plots and can better be studied based on the dQ/dU profiles shown in Figure 6c. According to Song the presence of cation order is reflected in the gap between the two Ni-related peaks in the dQ/dU plot. In both disordered samples d-LNMO-48 and d-LNMO-44, a gap of 58 mV is found between the Ni^{2+}/Ni^{3+} plateau and the Ni^{3+}/Ni^{4+} plateau, which corresponds exactly to the value for disordered LNMO reported by Casas–Cabanas.[33] In the same study, for two well ordered LNMO materials, a decrease of the voltage gap down to 21 mV was found, which is close to the value observed for the highly ordered o-LNMO-49 sample ($\Delta V_{\text{Ni–Ni}} = 19$ mV). The Mn(III) rich ordered material o-LNMO-43 has a voltage gap of 42 mV, which is close to the value of 47 mV for the OO670 sample investigated in Casas–Cabanas study. For the latter, based on the lattice parameter, an increased Mn(III) content is well conceivable and a high degree of cation order was confirmed by means of neutron powder diffraction.[33] The observed voltage gaps are also in good agreement with values reported by Liu et al.[42] and confirm the classification as a (partially) ordered material. Whether the different gaps in samples 1 and 4 are a result of different degrees of cation order or are mainly due to the different Mn(III) content cannot be clarified on the basis of the available data. A possible relation between cation order and LNMO composition is discussed in Section 4.4. We find voltage gaps in the discharge profiles which are 2 to 7 mV smaller compared to the gaps of the charge profiles. The differences between the individual half cycles thus are comparatively small, as previously 6 to 27 mV were reported.[42] Another interesting feature of the dQ/dU plots is the voltage drop between the charge and discharge profiles, which was derived from the position of the Ni^{3+}/Ni^{4+} peaks. The values are noted as ΔV in Figure 6c. At 0.05 C the voltage drops by 41 mV for o-LNMO-49. For samples
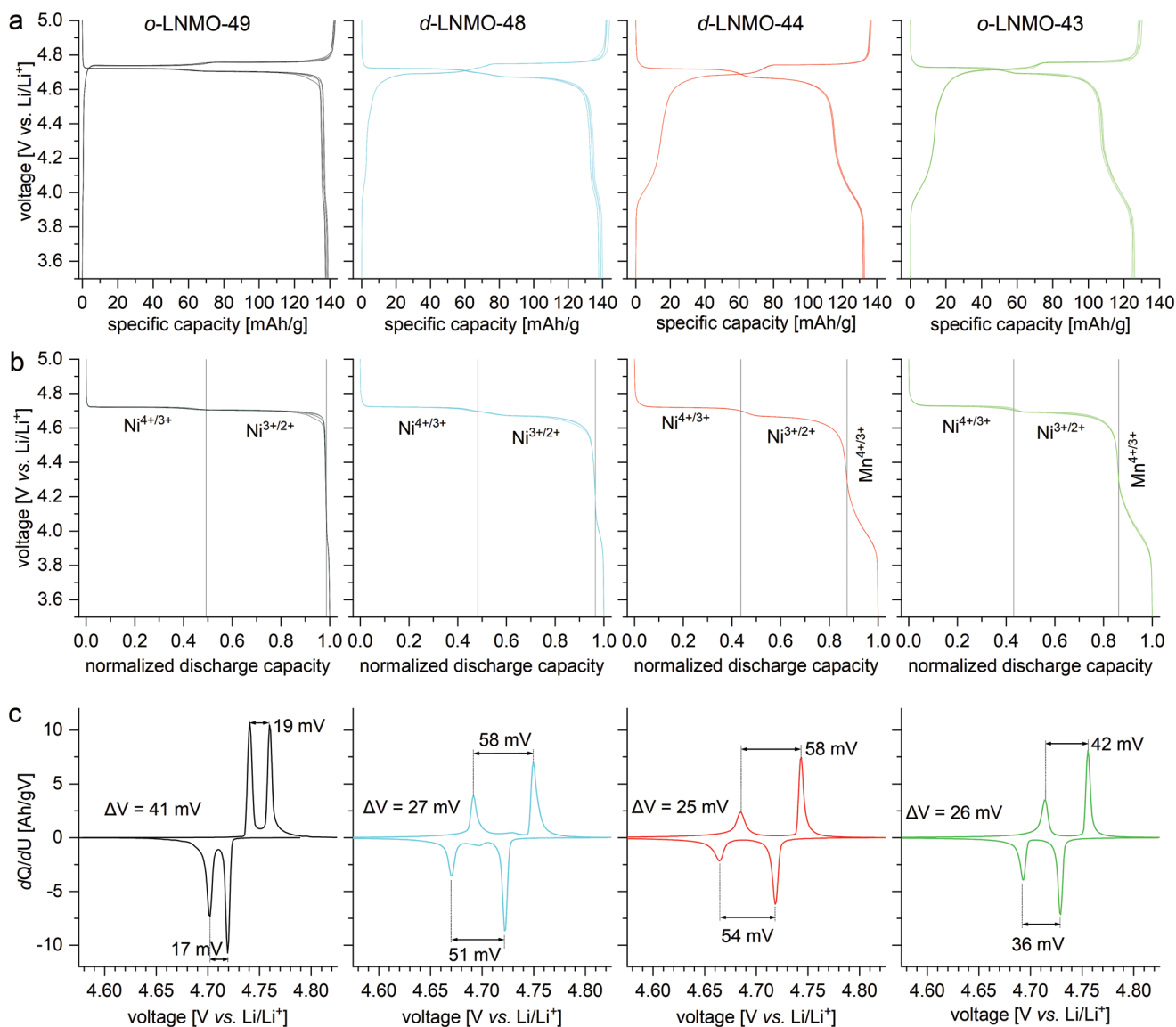
Figure 6. a) Voltage profiles during the second cycle with a rate of 0.05 C. Based on the pronounced step around 4 V the Mn-related redox contribution becomes obvious from the profiles of the Ni-deficient LNMO phases d-LNMO-44 and o-LNMO-43. b) Normalized discharge profiles of the second cycles. The voltage profiles of all four cells are shown in each subfigure, highlighting the high consistency of the profiles. c) dQ/dU plots derived from the voltage profile of a single cell (second cycle, 0.05 C). In the disordered samples, voltage gaps of 51–58 mV between the two nickel potentials are found, in the (partially) ordered samples reduced gaps are found. The voltage polarisation ΔV is increased only for o-LNMO-49.

2, 3, and 4, in contrast, very similar voltage lowerings of 27, 25, and 26 mV are observed between the charge and discharge voltage. This trend continues and intensifies at higher C-rates,

as can be seen from the corresponding voltage profiles for 0.5, 1, 2, and 5 C which are depicted in Figure S5, Supporting Information. The increased voltage drop of o-LNMO-49 could

Table 5. Discharge profile evaluation of samples 1–4 (second cycle, 0.05 C) yielding the compositions of the LNMO phases. The stoichiometric coefficients $\nu(Ni)$ and $\nu(Mn)$ are calculated according to Equations (8) and (9).

	Sample	Capacity [mAh g⁻¹]	Redox activity contribution				Composition LiNi$_{0.5-x}$Mn$_{1.5+x}$O$_4$		
			Ni(sum)	Ni$^{4+/3+}$	Ni$^{3+/2+}$	Mn$^{4+/3+}$	ν(Ni)	ν(Mn)	Formula
1	o-LNMO-49	138.2(6)	98.7%	47.7%	51.0%	1.3%	0.494	1.506	LiNi$_{0.494}$Mn$_{1.506}$O$_4$
2	d-LNMO-48	138.9(8)	96.5%	49.4%	47.1%	3.5%	0.483	1.517	LiNi$_{0.483}$Mn$_{1.517}$O$_4$
3	d-LNMO-44	132.5(3)	87.3%	45.0%	42.3%	12.7%	0.437	1.563	LiNi$_{0.437}$Mn$_{1.563}$O$_4$
4	o-LNMO-43	125.2(6)	86.2%	43.0%	43.3%	13.8%	0.431	1.569	LiNi$_{0.431}$Mn$_{1.569}$O$_4$
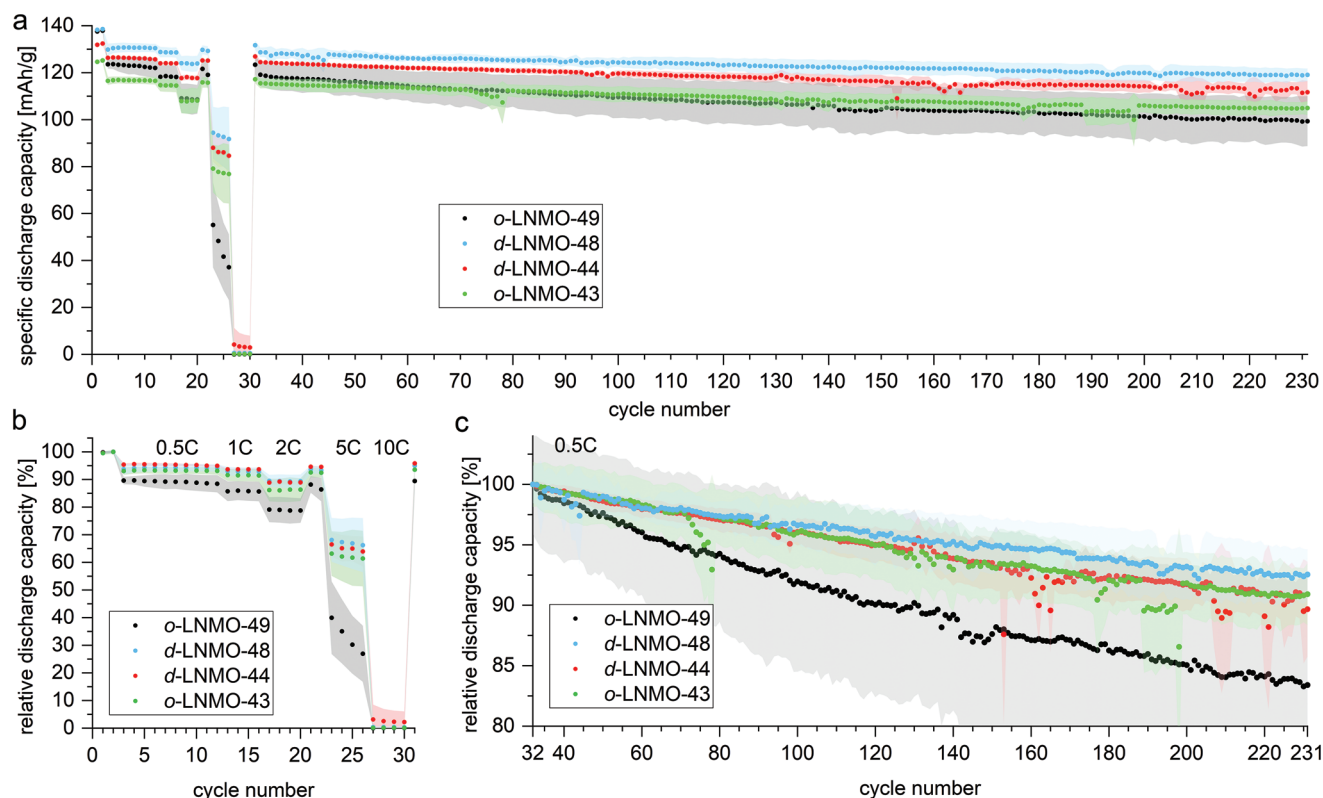
Figure 7. a) Specific discharge capacities and relative discharge capacities of the four different LNMO materials. For each material, the best three cells were evaluated. Each dot represents the mean value of these three cells, the error range represents the standard deviation of the three individual values. b) Relative discharge capacities during the rate capability test (100% reference: cycle number 2). c) Relative discharge capacities during the cycling stability test (100% reference: cycle number 32). The raw data, that is, the specific discharge capacities of the individual cells, is shown in Figure S6, Supporting Information.

be considered a direct indication for a different lithiation and delithiation mechanisms of o-LNMO-49 compared to the other three samples (see below).

The rate capabilities and cycling stabilities of the LNMO materials are shown in **Figure 7**. Relative discharge capacities during initial cycles at 0.5 C and the rate capability test are shown in Figure 7b. The relative discharge capacity clearly shows that samples 2–4 (d-LNMO-48, d-LNMO-44, and o-LNMO-43) show very similar cycling behavior. During the rate capability test, discharge capacities around 94%, 93%, 88%, and 65% of the starting capacity are obtained for these samples at C-rates of 0.5 C, 1 C, 2 C, and 5 C. The ordered o-LNMO-49 material, in contrast only provides around 89%, 86%, 79%, and 32%, which means that the relative capacity reduction is roughly doubled for each C-rate. None of the materials is capable to deliver a noteworthy capacity at a discharge rate of 10 C. This shows that LNMO clearly does not reach the performance of doped analogues such as LNMFTO (LiNi$_{0.48}$Mn$_{1.41}$Fe$_{0.1}$Ti$_{0.03}$O$_{3.95}$), where capacities of 92% and 88% of the starting capacity were obtained for 5 C and 10 C, despite larger primary particles and reduced specific surface.[26]

The cell degradation after 200 discharge cycles becomes obvious from Figure 7c. The best capacity retention is observed for d-LNMO-48 (92.5% capacity retention), closely followed d-LNMO-44 and o-LNMO-43, both with very similar capacity retentions around 90.5%. It is difficult to say whether the small difference to d-LNMO-48 can be attributed to Mn(III), the secondary

phase content, or is a random effect. The worst cycling stability of o-LNMO-49 however, is clearly visible from the data, as only 83% of the initial capacity is available after 200 cycles. The most plausible cause could be the different transformations mechanisms during the charging and discharging process. For close to stoichiometric ordered LNMO phases, two consecutive two phase reactions (LiNi$_{0.5}$Mn$_{1.5}$O$_4$ ⇆ Li$_{0.5}$Ni$_{0.5}$Mn$_{1.5}$O$_4$ ⇆ Ni$_{0.5}$Mn$_{1.5}$O$_4$) have been reported,[39] and it is assumed, that these two phase reactions accelerate the capacity decay.[43,44] Disordered Mn(III) rich LNMO in contrast, shows solid solution behavior (e.g., Li$_{1-x}$Ni$_{0.45}$Mn$_{1.55}$O$_4$ with $0 < x < 0.5$), in the first step of the (dis) charge process.[15,39] Based on the cycling data, and in agreement with the findings of Fehse,[16] it seems reasonable to assume that the lithiation and delithiation mechanism of the (partially) ordered o-LNMO-43 is similar to the one reported for disordered spinel phases. This issue, however, will be investigated in a subsequent study, together with LNMO versus graphite full cells, which allow for a better assessment of the capacity retention.

4. Discussion

4.1. An Extended Classification for LNMO Materials

From the above findings, it becomes obvious, that the standard classification solely as "ordered" and "disordered" LNMO is

misleading and does not cope with the complexity of LNMO phases. Therefore, we suggest an extended classification of LNMO materials taking into account the nickel content of the spinel phase. Similar to the NCM-classification, we propose adding the nickel content as a suffix, according to "LNMO-x" where x represents Ni in the general formula $LiNi_xMn_{2-x}O_4$. Materials of stoichiometric LNMO ($LiNi_{0.50}Mn_{1.50}O_4$) thus would be described as "LNMO-50," while typical materials containing Ni-deficient LNMO phases would be described, for example, as "LNMO-47" for $LiNi_{0.47}Mn_{1.53}O_4$. Prefixes like o and d for "ordered" and "disordered" should be used as usual, whenever these properties are known. If only the sample composition based on the starting materials is taken into account, this should always be stated, since calcination virtually always leads to a secondary phase formation, changing the actual composition of the spinel phase.

4.2. LNMO Sample and Spinel Phase Composition

As a consequence of the secondary phase formation during calcination (cf. Equations (2) and (3)) the composition of a LNMO material, that is, the cathode active material samples as a whole, usually differs from the composition of the corresponding spinel phase. The amounts of the constitutes Li, Ni, Mn, and O in the LNMO samples presented herein certainly are the same, apart from minor deviations in the oxygen content. Just like for most LNMO materials presented in literature, as a result of the starting material composition, $n_{Li}:n_{Ni}:n_{Mn}:n_O \approx 1:0.5:1.5:4-\delta$ uniformly applies. Nevertheless, LNMO materials literally always consist of at least two phases and notations like "$LiNi_{0.5}Mn_{1.5}O_{4-\delta}$" should be avoided, as they wrongly suggest the presence of a uniform compound.

The spinel phase composition, in contrast, can precisely be described as $LiNi_{0.5-x}Mn_{1.5+x}O_4$. Based on our LNMO samples and countless well executed studies on LNMO materials, it becomes evident, that the composition of the LNMO spinel phase is critical for the understanding of the electrochemical properties of LNMO materials. The composition of the spinel phase can be determined based on neutron power diffraction (NPD),[10,11,14–16] based on the LNMO lattice parameter[18,45] or based on voltage profile evaluation.[18,26,45]

To the best of our knowledge, so far no reliable evidence was brought forth, that would prove a significant effect of cation order on the lattice parameter of LNMO, or that would quantify the latter. The effect of the Ni content on the size of the unit cell, in contrast is proven beyond any doubt. Both, the studies of Zhong[18] and Kunduraci[45] show almost linearly decreasing lattice parameters for an increasing Ni content in LNMO. The samples investigated in this study are consistent with these findings. The reasonable assumption of Vegard behavior allows for a rough estimation of the Ni content of the spinel phase based on the variation of the lattice parameters. As discussed before,[27] PXRD data from different studies is difficult to compare. Relative differences of LNMO materials published within individual studies, in contrast, are quite reliable, as it can be assumed that uniform measurement conditions and evaluation techniques were used. The lattice parameter differences

thus can be used to estimate the relative differences in the Ni-content of LNMO phases within many studies. For random LNMO compositions $LiNi_{a-x}Mn_{(2-a)+x}O_4$ ($0 < a < 0.5$), the data of Zhong,[18] suggests a reduction of the nickel content by $x \approx 0.074$ for each pm lattice parameter increase.

The analysis of discharge profiles provides another simple and more accurate method for determining the LNMO composition, which, however has hardly been used in the past. Among the few exceptions are the works of Dahn,[18] Kunduraci,[45] and our previous work.[26] To estimate the LNMO phase composition, discharge profiles measured at low C-rates (e.g., 0.1 C) should be analyzed. Charge profiles tend to be distorted by parasitic side reactions. The assignment of the capacity to individual redox pairs can be made along demarcation lines at certain voltages, as shown before.[18,26,45] In addition to fixed threshold values for the assignment of partial capacity to Ni and Mn redox processes, the position of the inflection points of the discharge profiles can be analyzed as well. The stoichiometric coefficients $v(Ni)$ and $v(Mn)$ are calculated according to Equations (8) and (9):

$$v(Ni) = \frac{\text{Ni related capacity}}{2 \times \text{total capacity}} \tag{8}$$

$$v(Mn) = 2 - v(Ni) \tag{9}$$

Several studies including both, NPD and electrochemical characterization, show almost perfect agreement between the compositions determined by neutron diffraction and the compositions resulting from the voltage profiles. The comparable data, however is limited by the circumstance that in some neutron diffraction studies the Ni:Mn ratios of LNMO are constrained to certain values for some[10] or all[14] LNMO specimens or missing voltage profiles.[15] **Table 6** shows the compositions of LNMO phases published in well executed experimental studies, together with the composition resulting from our evaluation of the corresponding discharge profiles.

The remarkable consistency between the spinel phase compositions obtained by means of NPD and by the voltage profile evaluation emphasizes, that both methods are highly suitable to determine the LNMO phase composition. However, while access to neutron diffraction experiments is limited, the evaluation of the voltage profiles is feasible with standard laboratory equipment and basic testing hardware.

4.3. Mn(III) Content in LNMO

The Mn(III) content of the LNMO plays a central role for the degradation of LNMO graphite full cells.[46,47] The content of Mn(III) in the spinel phase, which can be precisely quantified, is a good approximation for the total content of Mn(III) of LNMO samples, as the secondary phase usually only accounts for minor phase fractions and contains little manganese.[11] Based on the spinel phase composition $LiNi_{0.5-x}Mn_{1.5+x}O_4$, and the oxidation states Li^I, Ni^{II}, and O^{-II}, as result of charge balancing, Mn(III) and Mn(IV) are found according to $LiNi_{0.5-x}Mn_{1.5-x}^{IV}Mn_{2x}^{III}O_4$. The Mn(III) content therefore results

**ADVANCED
SCIENCE NEWS**

www.advancedsciencenews.com

**ADVANCED
ENERGY
MATERIALS**

www.advenergymat.de

Table 6. LNMO phase compositions determined by means of synthesis or NPD in comparison with the compositions obtained by the voltage profile analysis.

	Original work			Voltage profile evaluation				
Sample	Source	Method	Composition	$Mn^{3+/4+}$	$Ni^{2+/3+/4+}$	ν(Ni)	ν(Mn)	Composition
Sample23	[18]	Synthesis	$LiNi_{0.5}Mn_{1.5}O_4$	0%	100%	0.5	1.5	$LiNi_{0.50}Mn_{1.50}O_4$
Sample22	[18]	Synthesis	$LiNi_{0.4}Mn_{1.6}O_4$	20.5%	79.5%	0.398	1.602	$LiNi_{0.40}Mn_{1.60}O_4$
Sample21	[18]	Synthesis	$LiNi_{0.3}Mn_{1.7}O_4$	43.4%	56.6%	0.283	1.717	$LiNi_{0.28}Mn_{1.72}O_4$
Sample20	[18]	Synthesis	$LiNi_{0.2}Mn_{1.8}O_4$	62.9%	37.1%	0.186	1.814	$LiNi_{0.19}Mn_{1.81}O_4$
Sample19	[18]	Synthesis	$LiNi_{0.1}Mn_{1.9}O_4$	81.3%	18.7%	0.093	1.907	$LiNi_{0.09}Mn_{1.91}O_4$
Ordered-LNMO	[10]	NPD	$LiNi_{0.44}Mn_{1.56}O_{4-\delta}$	11.8%	88.2%	0.441	1.559	$LiNi_{0.44}Mn_{1.56}O_4$
LNMO-900	[11]	NPD	$LiNi_{0.43}Mn_{1.57}O_4$	13.9%	86.1%	0.431	1.569	$LiNi_{0.43}Mn_{1.57}O_4$
LNMO-800	[11]	NPD	$LiNi_{0.45}Mn_{1.55}O_4$	10.0%	90.0%	0.450	1.550	$LiNi_{0.45}Mn_{1.55}O_4$
LNMO-D	[16]	NPD	$LiNi_{0.42}Mn_{1.58}O_4$	15.7%	84.3%	0.422	1.578	$LiNi_{0.42}Mn_{1.58}O_4$
LNMO-O	[16]	NPD	$LiNi_{0.45}Mn_{1.55}O_4$	12.9%	87.1%	0.436	1.564	$LiNi_{0.44}Mn_{1.56}O_4$

from the stoichiometric coefficients of Mn according to Equation (10)

$$\chi\left(Mn^{III}\right) = \frac{\nu\left(Mn^{III}\right)}{\nu\left(Mn^{III}\right) + \nu\left(Mn^{IV}\right)} \qquad (10)$$

The Mn(III) content of the spinel phase can therefore be precisely derived from the composition, which, in turn, is derived from the Mn(III) related redox activity contribution, as shown above. The Mn(III) contents calculated for samples 1–4 are shown in **Table 7**.

4.4. Formation of Cation Order in LNMO

As discussed above, cation ordering and Mn(III) content are independent properties of LNMO spinel phases.[10,14,26] However, it was often assumed that these properties were linked to each other. As a result, and as a consequence of common synthesis routes, most "ordered" materials discussed in literature are made up of LNMO phases which are close to the ideal composition $LiNi_{0.5}Mn_{1.5}O_4$ and thus contain Mn(IV) almost exclusively. "Disordered" samples, in contrast usually contain Mn(III) rich LNMO phases in the composition range between $LiNi_{0.47}Mn_{1.53}O_4$ and $LiNi_{0.42}Mn_{1.58}O_4$ (i.e., LNMO-47 to LNMO-42).

On the atomic scale, Ryoo found, that the formation of cation order in LNMO spinel phases requires Frenkel defects to occur.[48] It was also shown that these defects do not appear at temperatures below 500 °C. The study of Aktekin suggests that the minimum temperature for the disorder to order transition

$(T_{D\rightarrow O})$ is around 530 °C,[10] and in a previous study on Fe–Ti doped LNMO, a similar onset temperature for cation ordering was found in the range 540 to 580 °C.[26] The high degree of cation order in o-LNMO-49 was obtained during a holding step of 20 h at 680 °C in ambient atmosphere. The calcining temperature was chosen well below the frequently specified order to disorder transition temperature $(T_{O\rightarrow D})$ in the range of 700 to 730 °C[45] and below the LNMO decomposition temperature reported to be in the range of 690 to 695 °C when calcined in air.[10] Heating o-LNMO-49 to 750 °C for 30 min, which is slightly above $T_{O\rightarrow D}$, yields the d-LNMO-48. Beside the absence of cation order, it has a slightly higher Mn(III) content in the spinel phase, due to a not fully reversible secondary phase formation. Interestingly, calcining the Mn(III) rich sample d-LNMO-44 in the absence of oxygen at 650 °C for 18 h in an argon atmosphere, did not yield an ordered LNMO phase with similar Mn(III) content. Instead, a disordered LNMO phase with drastically increased lattice parameter and secondary phase fraction was obtained. This indicates that for this d-LNMO-44 spinel both, the decomposition temperature and $T_{O\rightarrow D}$ are shifted below 650 °C. Repeating the calcining of d-LNMO-44 at 600 °C for 18 h under argon, the formation of cation order was observed and sample o-LNMO-43 was obtained in which the secondary phase fraction was only slightly increased. This on one hand is fully consistent with the finding of Aktekin, who reported the order–disorder transition temperature for a sample with similar LNMO composition $(LiNi_{0.44}Mn_{1.56}O_4)$ to be around 630 °C.[10] On the other hand, this also demonstrates that there is not a specific order–disorder transition temperature for LNMO phases. Instead, $T_{O\rightarrow D}$ seems to be reduced for $LiNi_{0.5-x}Mn_{1.5+x}O_4$ with increasing Mn content and x-values.

Table 7. Calculation of the Mn(III) content of the spinel phase for the four different LNMO materials (fully lithiated state).

	Sample	$Mn^{4+/3+}$ related redox contribution	Spinel composition	Balanced composition	$\chi(Mn^{III})$
1	o-LNMO-49	1.3%	$LiNi_{0.494}Mn_{1.506}O_4$	$LiNi_{0.494}Mn^{III}_{0.012}Mn^{IV}_{1.494}O_4$	0.8%
2	d-LNMO-48	3.5%	$LiNi_{0.483}Mn_{1.517}O_4$	$LiNi_{0.483}Mn^{III}_{0.034}Mn^{IV}_{1.483}O_4$	2.1%
3	d-LNMO-44	12.7%	$LiNi_{0.437}Mn_{1.563}O_4$	$LiNi_{0.437}Mn^{III}_{0.126}Mn^{IV}_{1.437}O_4$	8.1%
4	o-LNMO-43	13.8%	$LiNi_{0.431}Mn_{1.569}O_4$	$LiNi_{0.431}Mn^{III}_{0.138}Mn^{IV}_{1.431}O_4$	8.8%

From a crystallographic point of view, a gradual decrease of the highest possible extend of cation order must be expected with increasing x in LiNi$_{0.5-x}$Mn$_{1.5+x}$O$_4$. The ideal ordered crystal structure requires a Ni:Mn ratio of 1:3 in order to fully occupy the 4a and 12d Wyckoff position of space group $P4_332$ with nickel and manganese. With a decreasing nickel content, the admixture of manganese on the 4a sites inevitably occurs. In o-LNMO-43 the Ni:Mn ratio is reduced to 0.86:3.14, which means that at least 14% of the 4a positions are occupied with manganese ions. This inevitably leads to distortions of well-ordered crystal domains in LNMO and it appears reasonable to refer to such Mn(III)-rich phases, as merely "partially ordered" instead of "ordered". Moreover, it can be assumed that the thermodynamic advantage of the ordered $P4_332$ phase compared to the disordered $Fd\bar{3}m$ phase gradually decreases with increasing Mn content, which might cause the decrease of $T_{O\rightarrow D}$. These findings finally suggest that the temperature range between $T_{D\rightarrow O}$ and $T_{O\rightarrow D}$ in which cation order increases, becomes smaller with increasing Mn(III) content, presumably mainly due to a decline of $T_{O\rightarrow D}$.

4.5. Relevance of Cation Order

The majority of research papers (e.g. refs. [33,49,50]) and review articles (e.g., refs. [1,43,47,51]) assume, that the cation order in general plays an important role for the electrochemical performance of LNMO materials. In agreement with this assumption, we do find accelerated degradation and significantly reduced rate capability for the ordered phase o-LNMO-49, which contains Mn(IV) almost exclusively. Nevertheless, we would like to put this into perspective and advocate the point of view that the high relevance of cation order is limited to a rather small range of spinel phase compositions, namely those with ideal or close to ideal composition LiNi$_{0.5}$Mn$_{1.5}$O$_4$, corresponding to a Ni:Mn ratio of 1:3. Accordingly, in a study on several Fe–Ti doped LNMO materials, it was found that the cation order, had virtually no effect on the rate capability and cycling performance of these materials.[26] Results contradicting a general importance of cation order in LNMO were likewise recently reported by de Geranno[52] and Fehse[16] who investigated Ni-deficient LNMO materials. The same applies for the Mn(III) rich (partially) ordered and disordered o-LNMO-43 and d-LNMO-44 investigated herein. Both show similar rate capabilities and cycling stabilities in the half cell and we were not able to identify any significant influence of the cation ordering regarding half cell degradation. A reasonable explanation for the similar cycling behavior was likewise provided by Fehse.[16] It was found that both, predominantly ordered and predominantly disordered Mn(III) rich LNMO materials show a largely similar reaction process and electronic and local structural evolution. Therefore, from previous studies[16,26,52] and the experimental results of this work, it becomes evident, that cation order is of great importance only for LNMO phases close to the ideal composition.

4.6. High Temperature Phase Transitions

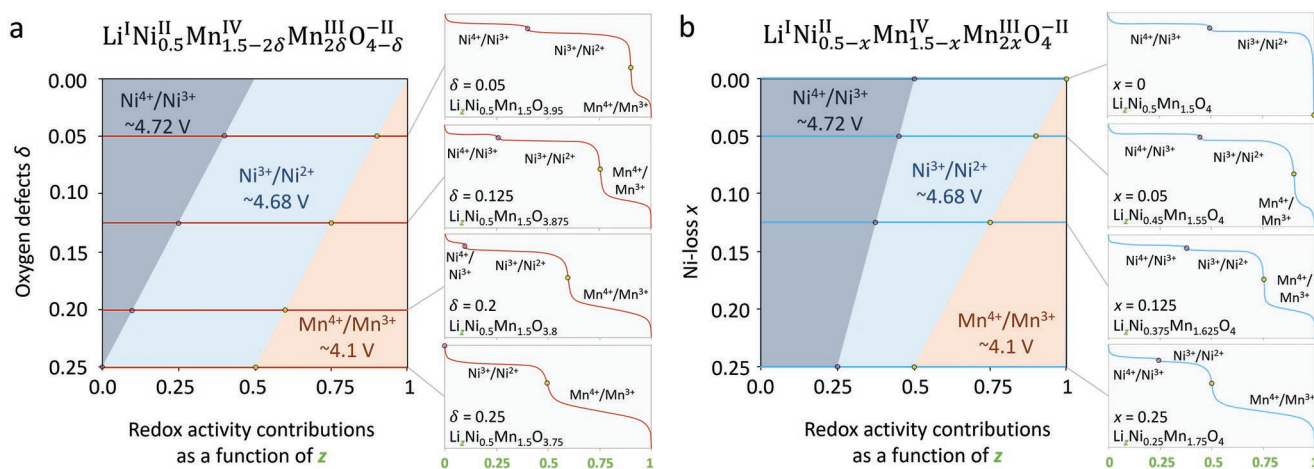The diffraction patterns recorded at temperatures of 800 to 1000 °C reveal a significant increase of the 200 and 422 reflections, which indicates partial occupation of the tetrahedral positions of the spinel phase with transition metal ions. To the best of our knowledge, this effect has not been reported or discussed in previous studies.[14] We see a need for further investigations and consider a more complex phase transition mechanism than the one suggested by Song.[17] Our data indicates, that at high temperatures, major parts of the lithium ions initially present in the spinel phase are transferred to the secondary phase, which in turn should be rather Li-rich. This means that during crystal growth, which takes place almost exclusively at high temperatures, strongly deviating phases and phase balances are involved. The commonly observed phase fractions and compositions are formed very lately in the calcining process during the cooling steps. This also fits with the finding, that the electrochemical properties of LNMO materials can be controlled very well via the cooling rates and tempering steps, as shown above and reported before.[26]

4.7. Secondary Phases in LNMO

The diffraction patterns of the Mn(III) rich LNMO materials d-LNMO-44 and o-LNMO-43 reveal the presence of additional secondary phase reflections and hence none of these phases can be properly described as a simple rocksalt phase with a small 414 pm unit cell. The mere existence of superstructure reflections originating from an ordered rock salt phase is a clear indication that the secondary phases of LNMO materials contain manganese ions, as for pure Li$_x$Ni$_{1-x}$O phases, these reflections have not been reported.[23,24] The classification of the minor phases in LNMO samples remains challenging because of the low phase fractions and the severe reflection overlap with LNMO. Therefore diffraction data with good counting statistics and a careful data analysis are required. In most studies, the secondary phase is described as a simple rocksalt phase, which might originate from the fact that, the low indexed reflections of the larger unit cells are rather difficult to detect. Nevertheless, in some studies with strong focus on diffraction techniques, some secondary phases were clearly identified as ordered rocksalt phases[25] or Ni-rich layered compounds.[26] It is likely that the stronger the spinel phase is depleted of nickel, the more manganese is incorporated in the formed secondary phase. Based on both, the LNMO composition and significantly reduced LNMO discharge capacities compared to the theoretical capacity of 146.8 mAh g^{-1}, we assume that many studies underestimate the phase fractions of the secondary phases in their materials. A detailed discussion of the relationship between the secondary phase fraction, LNMO composition and discharge capacity is given in Section 4.9.

4.8. Overcoming the Concept of Oxygen Defects

As mentioned above, the existence of oxygen defects in the spinel phase has been doubted previously.[11,16,18] Herein we provide additional evidence contradicting the idea of oxygen defects. Assuming that the composition and structure of the LNMO phase determines the voltage profile, it can be shown that oxygen defects may not occur at all, or only to a negligible

ADVANCED
SCIENCE NEWS
www.advancedsciencenews.com

ADVANCED
ENERGY
MATERIALS
www.advenergymat.de

Figure 8. Redox activity distribution and schematic discharge profiles based on different LNMO charge balancing mechanisms. a) Charge balancing via oxygen defects: Ni no longer can be fully oxidized to Ni(IV) leading to a narrower Ni^{4+}/Ni^{3+} discharge plateau (not reported in literature). b) Charge balancing resulting from nickel loss: Both Ni redox couples equally contribute to the total Ni related capacity. All Ni is oxidized to Ni(IV).

extent. We already analyzed the implications of the two charge balancing mechanisms on the voltage profiles of Fe–Ti doped LNMO materials, and suggested the depletion of Ni as the predominant cause for charge balancing.[26] Herein, further evidence is provided that the same applies for undoped LNMO. As illustrated schematically in **Figure 8**a, for an increasing amount of oxygen defects, according to the formula suggested by Pasero[12] ($LiNi_{0.5}Mn_{1.5}O_{4-\delta}$), a continuous shrinkage of the $Ni^{4+/3+}$ redox plateau would be expected during delithiation. The $Ni^{2+/3+}$ plateau in contrast, should keep a redox capacity accountable for 50% of the total capacity for $0 < \delta < 0.25$. If one assumes nickel loss as the predominant cause for the reduction of Mn(IV) and a mechanism according to $LiNi_{0.5-x}Mn^{IV}_{1.5-x}Mn^{III}_{2x}O_4$, both Ni plateaus should contribute equally to the total Ni related capacity, as shown in Figure 8b.

The experimental normalized voltage profiles of the LNMO materials investigated in this study are shown in Figure 6b. They are consistent with the calculated positions for the voltage steps based on charge balancing resulting from Ni-loss, which are shown by vertical lines. Similar coincidences are found for Fe–Ti doped LNMO,[26] a study on LNMO materials $LiNi_xMn_{2-x}O_4$ ($0.50 \geq x \geq 0.36$) by Kunduraci,[45] or the studies of Aktekin[10] and Fehse.[16] In all these studies, the two different Ni plateaus are sufficiently clearly distinguishable. Hence, the voltage profiles of all the aforementioned studies are in good agreement with a charge balance according to $LiNi_{0.5-x}Mn^{IV}_{1.5-x}Mn^{III}_{2x}O_4$ and show no evidence for the existence of oxygen defects. We have not been able to find voltage profiles in the literature that clearly correspond to those shown in Figure 8a.
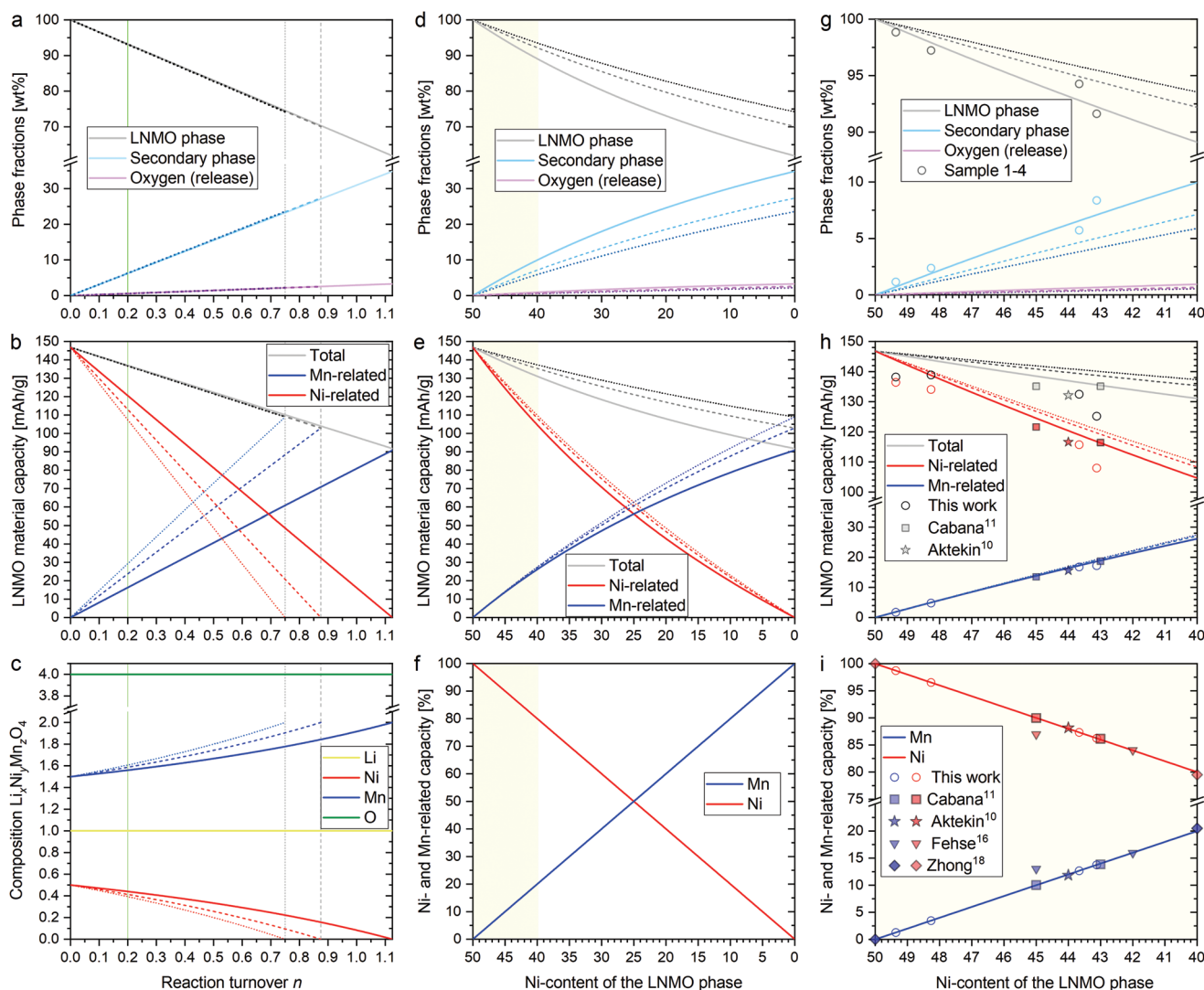
A second experimental evidence that no oxygen defects are to be found in LNMO is the good agreement between the mass losses reported in several TGA studies with the specimen mass losses resulting from the spinel and rocksalt phase fractions obtained by the high temperature XRD study (cf. Figure 5c,f). Aktekin found a mass loss of about 1.4 wt% when heating LNMO in air to 780 °C,[10] which is in good agreement with the loss of roughly 1.5–2 wt% calculated from the diffraction patterns recorded at 800 °C. For 900 and 1000 °C, the high temperature

XRD study suggests a mass loss of roughly 4–5.5 wt% and 5.5–7 wt% depending on the individual pattern and the secondary phase model used in the refinement (see above). These results are fully consistent with the TGA mass losses of 5.5 wt% for 900 °C reported by Song[17] and the loss of 7 wt%, which was consistently reported by Pasero and Cai.[12,14] It is therefore highly likely, that the mass losses observed during high temperature treatments of LNMO materials are caused by the formation of the side phase and not by oxygen defects in the spinel phase.

We do not doubt that some point defects of the oxygen lattice can exist in LNMO and we also assume that the substitution of Mn(IV) by trivalent ions like Fe(III)[26] or Ga(III)[53] might favor quantitative oxygen defect formation. However, we want to emphasize that oxygen defects are clearly not directly related to the Mn(III) content in LNMO materials. Hence, for a better understanding of LNMO materials, we believe that the concept of oxygen defects should be overcome.

4.9. Modeling the Properties of LNMO Materials

Based on Equations (3)–(6), for every composition and phase fraction of the secondary phase, the composition of the LNMO phase and the theoretical capacity of the resulting LNMO material can be calculated. Thus, it becomes possible to predict key properties of the LNMO phase or the material based on varying assumptions on the side phase or the Ni-content of the spinel phase. In order to illustrate some predictions that can be made based on Equations (3)–(6), we considered three different secondary phases with lithium to transition metal ratio (Li:TM) of 1:2 and Ni:Mn ratios of 2:1 ($Li_{0.33}Ni_{0.44}Mn_{0.22}O$) and 6:1 ($Li_{0.33}Ni_{0.57}Mn_{0.10}O$) and a pure Li–Ni–O secondary phase ($Li_{0.33}Ni_{0.66}O$) for our calculations. Therefore, the secondary phase parameters were set to $a = 1/3$, and $b = 2/3$, 6/7, and 1, respectively. The outcome is shown in **Figure 9**. Herein, results for the secondary phase $Li_{0.33}Ni_{0.44}Mn_{0.22}O$ are shown by a solid line, those for $Li_{0.44}Ni_{0.57}Mn_{0.10}O$ by a dashed line and those for $Li_{0.33}Ni_{0.66}O$ by a dotted line.

**ADVANCED
SCIENCE NEWS**

www.advancedsciencenews.com
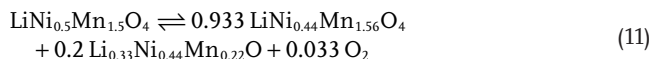
**ADVANCED
ENERGY
MATERIALS**

www.advenergymat.de

Figure 9. a–c) Calculated properties of LNMO materials based on Equations (3)–(6), as a function of the reaction turnover n and d–f) as a function of the Ni-content of the spinel phase. The results for the different side phase composition $Li_{0.33}Ni_{0.44}Mn_{0.22}O$, $Li_{0.33}Ni_{0.57}Mn_{0.10}O$, and $Li_{0.33}Ni_{0.66}O$ are indicated by a solid line, dashed line, and dotted line, respectively. g–i) Enlarged sections of (d–f), representing the composition range of typical LNMO spinel phases ($LiNi_{0.50}Mn_{1.50}O_4$ to $LiNi_{0.040}Mn_{1.60}O_4$). In addition, the experimental data of samples 1–4 and the data from studies listed in Table 6 was added, whenever comparability was given.

The phase fractions of LNMO, the secondary phase and the corresponding oxygen release are depicted in Figure 9a as a function of the turnover of the reaction n. As indicated by the *x*-axis boundary or the dashed and dotted vertical lines, in our examples n is limited to 1.125, 0.875, and 0.75. At these hypothetical maxima, the Ni rich secondary phase coexists beside a Ni-free "LNMO" material, that is, $LiMn_2O_4$ and thus, further reaction is not possible. The evolution of the LNMO phase compositions is illustrated in Figure 9c and the corresponding compositions for lower n values become visible. Figure 9b shows the theoretical capacity of LNMO materials, taking into account the mass of the electrochemically inactive secondary phase. It becomes obvious that the frequently cited capacity of 146.8 mAh g⁻¹ is the capacity of a pure-phase LNMO. For actual LNMO materials, where the reaction turnover n is always > 0, this capacity hardly can be reached, as the formation of

secondary phases during calcination leads to capacity loss. The Ni- and Mn-related redox activity, which is likewise shown in Figure 9b, results from the Ni-loss of the spinel phase and manifests itself by the additional voltage plateau around 4 V, as discussed above and shown in Figures 6b and 8b.

When for instance the secondary phase is $Li_{0.33}Ni_{0.44}Mn_{0.22}O$, as suggested by Cabana[11] and the reaction turnover $n = 0.2$ (green line in Figure 9a–c), a reaction according to Equation (11) is expected. A secondary phase fraction of ≈6.2 wt% is obtained and a LNMO composition of $LiNi_{0.44}Mn_{1.56}O_4$ should be found. As shown in Figure 9b, the capacity is expected to be reduced from 146.8 to 136.8 mAh g⁻¹, while voltage profiles with Ni- and Mn- related redox contributions of 88% and 12% are anticipated. As listed in Table 6, Aktekin found precisely this composition for the "ordered LNMO" sample.[10] The electrochemical investigation in a LNMO–LTO full cell yielded a

**ADVANCED
SCIENCE NEWS**

www.advancedsciencenews.com

**ADVANCED
ENERGY
MATERIALS**

www.advenergymat.de

reasonable capacity of 132 mAh g⁻¹ and exactly the same Ni- and Mn- related redox activities as predicted. This example emphasizes, that the general reaction Equations (3)–(6) is not a purely mathematical construct, but reflects very well the results of properly conduced experimental studies on LNMO.

$$\text{LiNi}_{0.5}\text{Mn}_{1.5}\text{O}_4 \rightleftharpoons 0.933\ \text{LiNi}_{0.44}\text{Mn}_{1.56}\text{O}_4$$
$$+ 0.2\ \text{Li}_{0.33}\text{Ni}_{0.44}\text{Mn}_{0.22}\text{O} + 0.033\ \text{O}_2 \qquad (11)$$

Since the reaction turnover n is a rather inaccessible parameter, it makes sense to calculate the properties of LNMO materials as a function of the Ni content of the spinel phase. The corresponding plots are shown in Figure 9d–f, with enlarged sections for LNMO-50 to LNMO-40, corresponding to the main phase composition $\text{LiNi}_{0.5}\text{Mn}_{1.5}\text{O}_4$ to $\text{LiNi}_{0.4}\text{Mn}_{1.6}\text{O}_4$ in Figure 9g–i. The experimental values of samples investigated in this work and of the reference samples listed in Table 4 were inserted and show good agreement with the theoretical values. As discussed above, the phase fractions of samples 1 to 4 correspond to the calculated values within their probable error range and are in good agreement with secondary phases with Ni:Mn rations of 2:1 or 6:1. The secondary phase fraction of sample 4 calcined in an argon atmosphere is increased, which, however, is to expect according to the removal of oxygen from the chemical equilibrium in Equation (3). The experimental capacities for the samples calcined in air are mostly 3 to 6 mAh g⁻¹ smaller compared to the rectified theoretical capacities, which we consider to be decent values for proper cell building. The relative discharge capacities shown in Figure 9f,i are independent from secondary phase fraction and overall capacity. Since the composition of the LNMO phases in samples 1–4 are derived from the voltage profiles, the values are exactly on the predicted lines for the Ni- and Mn-related redox activity in Figure 9f. However, the modeled predictions are also in very good agreement with relative discharge capacity distributions of the samples of Zhong,[18] Cabana[11] and Aktekin,[10] and Fehse,[16] listed in Table 6. We found only very few studies with results beyond the scope of our model limitations. In the composition range of common LNMO materials, that is, $\text{LiNi}_{0.5}\text{Mn}_{1.5}\text{O}_4$ to $\text{LiNi}_{0.4}\text{Mn}_{1.6}\text{O}_4$, we consider the agreement of our calculations with the independent experimental from Table 6 as a very strong indication for the correctness of Equations (3)–(6) and the underlying assumptions.

4.10. Possible Compositions for Future LNMO Materials

In the past two decades, materials with disordered LNMO phases and significant Mn(III) content (e.g., LNMO-42 to LNMO-46) have been preferred over materials with Ni-rich LNMO phases, such as, for example, LNMO-50 to LNMO-48, mainly due to the bad reputation of close to stoichiometric ordered LNMO. Beyond any doubt, compared to the latter, these Mn(III)-rich materials have significant advantages when cycled versus Li anodes, such as higher rate capability and long term cycling stability. On the other hand, calcining programs yielding high Mn(III) contents usually also yield high phase fractions of the electrochemically inactive secondary phase and thus lead to a capacity loss. Moreover, the favorable properties

of these materials are hardly transferrable to cells with graphite anodes, which is considered to be a perquisite for successful commercialization.[4] The poor full cell performance of these materials, is reported to result from Mn(III) disproportionation and subsequent dissolution and associated parasitic reactions.[46] From our point of view, it is therefore reasonable to focus on minimizing Mn(III) in LNMO materials, while maintaining disordered crystal structures. A promising experimental result regarding this, is that d-LNMO-48 outperforms all other samples investigated in this study. As a close to stoichiometric disordered LNMO material with a Mn(III) content of only 2.1%, it yields a decent discharge capacity of 138.9 mAh g⁻¹ and better long term cycling stability compared to a typical Mn(III) rich disordered material like d-LNMO-44 with 8.1% Mn(III) and a starting capacity of only 132.5 mAh g⁻¹.

5. Conclusion

On the basis of an analysis of the literature, the current knowledge on the solid state chemistry of LNMO was summarized and controversial issues on this cathode active material were addressed. Following considerations on the composition and crystallography of the LNMO phase and the secondary phases, and supported by new experimental findings as well as the findings of preceding studies, common assumptions on LNMO could be confirmed, rejected, or put into perspective. Therefore, a comprehensive and coherent understanding of LNMO is provided. More specifically, we were able to balance a general chemical equation for the formation of LNMO materials, which for the first time allows to calculate key electrochemical properties for different LNMO compositions and secondary phase fractions. The balanced equation provides a powerful tool check the plausibility of experimental data on LNMO materials and could help to figure out crucial parameters for the improvement of LNMO materials in subsequent studies. From different calcining programs, four different types of LNMO materials were obtained, including rather uncommon Mn(III) rich partially ordered, and Mn(IV) rich disordered spinel phases. To systematically categorize these materials, we suggest an extension of the classification of LNMO materials based on the spinel phase composition, where "d-LNMO-44" for example represents a material containing a disordered LNMO phase with the composition $\text{LiNi}_{0.44}\text{Mn}_{1.56}\text{O}_4$. If established, such a classification could help to better understand varying results of different LNMO materials and bring more comparability to the scientific debate. An in situ XRD study provides evidence, that during high temperature treatment, Li is largely transferred to the secondary phase. This emphasizes that the phase compositions and thus the LNMO material properties to a large extend can be controlled by tempering steps and cooling rates. It is confirmed, there is not a uniform rocksalt phase in LNMO materials, but that a variety of secondary phases with cubic or rhombohedral symmetry exist. Moreover, it is emphasized that the impact of cation ordering on the cycling behavior is most likely limited to close to stoichiometric spinel phase compositions. Furthermore, we provide new evidence that oxygen defects in the LNMO phase do not exist at all, or only to a negligible extend. We once again highlight that the compositions of LNMO phases reliably

can be derived from the discharge profiles, as we consider this approach to be of essential to gain a better understanding of LNMO. With *o*-LNMO-49 a material is presented, which seems to have the highest degree of cation ordering of the spinel phase reported so far. By briefly heating this material to 750 °C, *d*-LNMO-48 is obtained, which contains a close to stoichiometric disordered LNMO phase. The material provides a discharge capacity of 138.9 mAh g^{-1} and contains 2.1% Mn(III), which is only one-fourth of typical "disordered" LNMO materials. Due to its decent cycling stability, materials of this type should be suitable for the application in LNMO-graphite full cells.

Supporting Information

Supporting Information is available from the Wiley Online Library or from the author.

Conflict of Interest

The authors declare no conflict of interest.

Author Contributions

P.S.: Conceptualization, methodology, investigation, visualisation, supervision, writing—original draft, validation, writing—review and editing. V.M.: Supporting investigation and writing—review and editing. H.G.: Funding, supporting investigation, and writing—review and editing. J.B.: Resources, validation, writing—review and editing.

Data Availability Statement

The data that support the findings of this study are available from the corresponding author upon reasonable request.

[1] T.-F. Yi, J. Mei, Y.-R. Zhu, *J. Power Sources* **2016**, *316*, 85.
[2] M. Armand, P. Axmann, D. Bresser, M. Copley, K. Edström, C. Ekberg, D. Guyomard, B. Lestriez, P. Novák, M. Petranikova, W. Porcher, S. Trabesinger, M. Wohlfahrt-Mehrens, H. Zhang, *J. Power Sources* **2020**, *479*, 228708.
[3] D. Lu, M. Xu, L. Zhou, A. Garsuch, B. L. Lucht, *J. Electrochem. Soc.* **2013**, *160*, A3138.
[4] W. Li, Y.-G. Cho, W. Yao, Y. Li, A. Cronk, R. Shimizu, M. A. Schroeder, Y. Fu, F. Zou, V. Battaglia, A. Manthiram, M. Zhang, Y. S. Meng, *J. Power Sources* **2020**, *473*, 228579.
[5] A. Bhandari, J. Bhattacharya, *J. Electrochem. Soc.* **2017**, *164*, A106.
[6] P. Jehnichen, K. Wedlich, C. Korte, *Sci. Technol. Adv. Mater.* **2019**, *20*, 1.
[7] R. Jung, M. Metzger, F. Maglia, C. Stinner, H. A. Gasteiger, *J. Phys. Chem. Lett.* **2017**, *8*, 4820.
[8] G. Q. Liu, L. Wen, Y. M. Liu, *J Solid State Electrochem* **2010**, *14*, 2191.
[9] M. Hu, X. Pang, Z. Zhou, *J. Power Sources* **2013**, *237*, 229.
[10] B. Aktekin, M. Valvo, R. I. Smith, M. H. Sørby, F. Lodi Marzano, W. Zipprich, D. Brandell, K. Edström, W. R. Brant, *ACS Appl. Energy Mater.* **2019**, *2*, 3323.
[11] J. Cabana, M. Casas-Cabanas, F. O. Omenya, N. A. Chernova, D. Zeng, M. S. Whittingham, C. P. Grey, *Chem. Mater.* **2012**, *24*, 2952.
[12] D. Pasero, N. Reeves, V. Pralong, A. R. West, *J. Electrochem. Soc.* **2008**, *155*, A282.
[13] J. M. Tarascon, W. R. McKinnon, F. Coowar, T. N. Bowmer, G. Amatucci, D. Guyomard, *J. Electrochem. Soc.* **1994**, *141*, 1421.
[14] L. Cai, Z. Liu, K. An, C. Liang, *J. Mater. Chem. A* **2013**, *1*, 6908.
[15] L. Boulet-Roblin, D. Sheptyakov, P. Borel, C. Tessier, P. Novák, C. Villevieille, *J. Mater. Chem. A* **2017**, *5*, 25574.
[16] M. Fehse, N. Etxebarria, L. Otaegui, M. Cabello, S. Martín-Fuentes, M. A. Cabañero, I. Monterrubio, C. F. Elkjær, O. Fabelo, N. A. Enkubari, J. M. Del López Amo, M. Casas-Cabanas, M. Reynaud, *Chem Mater* **2022**, *34*, 6529.
[17] J. Song, D. W. Shin, Y. Lu, C. D. Amos, A. Manthiram, J. B. Goodenough, *Chem. Mater.* **2012**, *24*, 3101.
[18] Q. Zhong, A. Bonakclarpour, M. Zhang, Y. Gao, J. R. Dahn, *J. Electrochem. Soc.* **1997**, 205.
[19] C. F. Elkjær, J. Højberg, *Technical Status for Haldor Topsoe LNMO Material*, Haldor Topsoe, Copenhagen, Denmark **2021**.
[20] A. Feltz, J. Töpfer, B. Neidnicht, *Z. Anorg. Allg. Chem.* **1993**, *619*, 39.
[21] E. McCalla, J. R. Dahn, *Solid State Ionics* **2013**, *242*, 1.
[22] E. McCalla, A. W. Rowe, R. Shunmugasundaram, J. R. Dahn, *Chem. Mater.* **2013**, *25*, 989.
[23] W. Bronger, H. Bade, W. Klemm, *Z. Anorg. Allg. Chem.* **1964**, 188.
[24] W. Li, J. N. Reimers, J. R. Dahn, *Phys Rev B Condens Matter* **1992**, *46*, 3236.
[25] N. Kiziltas-Yavuz, M. Yavuz, S. Indris, N. N. Bramnik, M. Knapp, O. Dolotko, B. Das, H. Ehrenberg, A. Bhaskar, *J. Power Sources* **2016**, *327*, 507.
[26] P. Stüble, S. Indris, M. Müller, H. Geßwein, J. R. Binder, *J. Mater. Chem. A* **2022**, *10*, 9010.
[27] H. Geßwein, P. Stüble, D. Weber, J. R. Binder, R. Mönig, *J. Appl. Crystallogr.* **2022**, *55*, 503.
[28] P. Stüble, J. R. Binder, H. Geßwein, *Electrochem. Sci. Adv.* **2021**, *2*, e2100143.
[29] H. M. Rietveld, *J. Appl. Crystallogr.* **1969**, *2*, 65.
[30] H. G. Scott, *J. Appl. Crystallogr.* **1983**, *16*, 159.
[31] J. F. Bérar, P. Lelann, *J. Appl. Crystallogr.* **1991**, *24*, 1.
[32] B. Aktekin, F. Massel, M. Ahmadi, M. Valvo, M. Hahlin, W. Zipprich, F. Marzano, L. Duda, R. Younesi, K. Edström, D. Brandell, *ACS Appl. Energy Mater.* **2020**, *3*, 6001.
[33] M. Casas-Cabanas, C. Kim, J. Rodríguez-Carvajal, J. Cabana, *J. Mater. Chem. A* **2016**, *4*, 8255.
[34] W.-N. Wang, D. Meng, G. Qian, S. Xie, Y. Shen, L. Chen, X. Li, Q. Rao, H. Che, J. Liu, Y.-S. He, Z.-F. Ma, L. Li, *J. Phys. Chem. C* **2020**, *124*, 27937.
[35] R. Amin, I. Belharouk, *J. Power Sources* **2017**, *348*, 311.

[36] P. Jehnichen, C. Korte, *Anal. Chem.* **2019**, *91*, 8054.

[37] N. Amdouni, K. Zaghib, F. Gendron, A. Mauger, C. M. Julien, *Ionics* **2006**, *12*, 117.

[38] K. Miwa, *Phys. Rev. B* **2018**, *97*, 075143.

[39] M. Kunduraci, G. G. Amatucci, *J. Electrochem. Soc.* **2006**, *153*, A1345.

[40] H. Berg, J. O. Thomas Wen Liu Gregory, C. Farrington, *Solid State Ionics* **1998**, *112*, 165.

[41] M.-L.-P. Le, P. Strobel, C. V. Colin, T. Pagnier, F. Alloin, *J. Phys. Chem. Solids* **2011**, *72*, 124.

[42] H. Liu, X. Zhang, X. He, A. Senyshyn, A. Wilken, D. Zhou, O. Fromm, P. Niehoff, B. Yan, J. Li, M. Muehlbauer, J. Wang, G. Schumacher, E. Paillard, M. Winter, J. Li, *J. Electrochem. Soc.* **2018**, *165*, A1886.

[43] G. Liang, V. K. Peterson, K. W. See, Z. Guo, W. K. Pang, *J. Mater. Chem. A* **2020**, *8*, 15373.

[44] W. K. Pang, C.-Z. Lu, C.-E. Liu, V. K. Peterson, H.-F. Lin, S.-C. Liao, J.-M. Chen, *Phys. Chem. Chem. Phys.* **2016**, *18*, 17183.

[45] M. Kunduraci, G. G. Amatucci, *J. Power Sources* **2007**, *165*, 359.

[46] J.-H. Kim, N. P. Pieczonka, Z. Li, Y. Wu, S. Harris, B. R. Powell, *Electrochim. Acta* **2013**, *90*, 556.

[47] J. Chen, Z. Huang, W. Zeng, F. Cao, J. Ma, W. Tian, S. Mu, *ChemElectroChem* **2021**, *8*, 608.

[48] H. Ryoo, H. B. Bae, Y.-M. Kim, J.-G. Kim, S. Lee, S.-Y. Chung, *Angew. Chem., Int. Ed. Engl.* **2015**, *54*, 7963.

[49] J. Liu, A. Huq, Z. Moorhead-Rosenberg, A. Manthiram, K. Page, *Chem. Mater.* **2016**, *28*, 6817.

[50] J. Lee, C. Kim, B. Kang, *NPG Asia Mater.* **2015**, *7*, e211.

[51] W. Li, B. Song, A. Manthiram, *Chem. Soc. Rev.* **2017**, *46*, 3006.

[52] M. de Gennaro, B. Ganev, M. Jahn, M. Reynaud, M. Fehse, L. Otaegui, M. Cabello, S. Mannori, O. Rahbari, in *SAE Technical Paper Series, SAE International400 Commonwealth Drive*, Warrendale, PA, **2021**.

[53] G. Liang, E. Olsson, J. Zou, Z. Wu, J. Li, C.-Z. Lu, A. M. D'Angelo, B. Johannessen, L. Thomsen, B. Cowie, V. K. Peterson, Q. Cai, W. K. Pang, Z. Guo, *Angew. Chem., Int. Ed.* **2022**, *61*, 134.